FINDING STRATEGIES TO REGULATE PROPAGATION AND CONTAINMENT OF DENGUE VIA INVARIANT MANIFOLD ANALYSIS

DANA CONTRERAS-JULIO*, PABLO AGUIRRE†, JOSÉ MUJICA‡, AND OLGA VASILIEVA§

Abstract. Dengue, zyka and chikungunya are viruses transmitted to humans by Aedes aegypti mosquitoes. In the absence of medical treatments and efficient vaccines, one of the control methods is to introduce *Aedes aegypti* mosquitoes infected by the bacterium *Wolbachia* into a population of wild (uninfected) mosquitoes. The goal consists in achieving population replacement in finite time by driving the population of wild females towards extinction, while keeping *Wolbachia*-infected mosquitoes alive and persistent. We consider a competition model between wild *Aedes aegypti* female mosquitoes and those infected with Wolbachia. Our goal is to examine the basin of attraction of a desired equilibrium state which represents the population replacement. For this, we study how the stable manifold that forms the basin boundary of interest changes under parameter variation. To achieve this, we combine tools from dynamical systems and geometric singular perturbation theory with numerical continuation methods. This allows us to present a strategy to get the desired population replacement with a minimum amount of released infected mosquitoes in a human intervention by choosing an appropriate combination of initial conditions and parameter values. Secondly, we characterize traveling waves in a spatiotemporal extension of our model. To this aim, we propose a new method to calculate and visualize 3D invariant manifolds in a 4D dynamical system. In this way, we find uncountably many heteroclinic connections between stationary states (each associated with a wave front exhibiting the desired population replacement), as intersections of global invariant manifolds in the 4D phase space.

Key words. Dengue, Aedes aegypti, Wolbachia, invariant manifolds, slow-fast dynamics, traveling waves, heteroclinic orbits.

AMS subject classifications. 37N25, 34K19, 37M20, 34A26, 34D15, 35C07, 37C29.

1. Introduction. Dengue is an infectious disease caused by a virus that is transmitted by mosquitoes, mainly by *Aedes aegypti* [28, 57]. The infection causes flu-like symptoms, and sometimes evolves into a life-threatening condition called severe dengue or hemorrhagic dengue. It is a widespread infection that occurs in all regions of the planet's tropical climate. In recent years, transmission has increased predominantly in urban areas and has become a major public health problem [9, 29, 65]. Currently, more than half of the world's population is at risk of contracting the disease and this is why the prevention and control of dengue has been an issue of international importance [9, 57]. The virus is transmitted by the females of *Aedes aegypti* during bites when they feed on human blood. *Aedes aegypti* is an invasive mosquito widely distributed in urban and semi-urban areas of all tropical and subtropical regions around the world [23]. The presence and abundance of this mosquito species correlates strongly also with the persistence and proliferation of yellow fever, chikungunya and zika [6, 59].

Recently the release of female *Aedes aegypti* mosquitoes infected by the bacterium *Wolbachia* has been proposed as a promising strategy to control dengue and chikungunya (an approach that may be combined with the release of sterile mosquitoes [7, 8, 11, 25, 37]). Indeed, this bacterium drastically reduces the transmissibility of different arboviral infections when its transmitters carry it [24, 27, 54, 78], increasing the period of virus incubation or simply blocking the virus. Empirical evidence attests that the *Wolbachia* symbiont is maternally transmitted by the female insect to her eggs

---

*Department of Mathematics, The University of Auckland, Private Bag 92019, Auckland, New Zealand.

†Departamento de Matemática, Universidad Técnica Federico Santa María, Casilla 110-V, Valparaíso, Chile.

‡Departamento de Matemática, Universidad Técnica Federico Santa María, Casilla 110-V, Valparaíso, Chile.

§Departamento de Matemáticas, Universidad del Valle, Cali, Colombia.

Corresponding author: pablo.aguirre@usm.cl

(that are further developed as *Wolbachia*-carrying males and females) and also induces a particular reproductive phenotype known as *cytoplasmic incompatibility (CI)* [21, 23, 75]. The CI phenotype causes inviability of eggs originated from matings between *Wolbachia*-free females and *Wolbachia*-carrying males. Moreover, the offspring produced by a *Wolbachia*-carrying female always generates *Wolbachia*-infected individuals regardless of her mating with either infected or uninfected males (see Table 1).

Aedes aegypti offspring		
Adults	Infected ♀	Uninfected ♀
Infected ♂	**Infected**	**Inviable eggs**
Uninfected ♂	**Infected**	**Uninfected**

TABLE 1
Illustration of the CI reproductive phenotype and maternal transmission of Wolbachia.

Many scholars point out that *wMelPop* strain of *Wolbachia* induces maternal transmission rates and CI levels close to 100% in *Aedes aegypti* mosquitoes [52, 78]. The latter facilitates the infection spread among wild mosquito populations despite the loss of individual fitness produced by this particular strain in its carriers [52, 63, 79]. Thus, maternal transmission and CI-phenotype are key features that are present in all mathematical models describing *Wolbachia* invasion in wild mosquito populations; see for instance [10, 15, 17, 38, 56]. Furthermore, *Wolbachia* dynamics is always bistable in the sense that only one population (either wild or *Wolbachia*-infected) should ultimately survive and persist in the environment. The latter fully agrees with the *principle of competitive exclusion* [13, 55] and clearly indicates that the final outcome of competition between two populations depends on their relative densities or frequencies. The prime advantage of wild mosquitoes with respect to *Wolbachia*-carriers consists in their unaltered individual fitness, while *Wolbachia*-infected mosquitoes bear reproductive preeminence granted by the CI-phenotype and maternal transmission. Therefore, there exists a certain threshold in the proportion between the current sizes of wild and *Wolbachia*-infected populations of mosquitoes —usually referred to as "frequency of *Wolbachia* infection"— above which the invasion and stabilization of *Wolbachia* can be achieved and maintained. When relative density (or frequency) of wild mosquitoes is low, an uninfected female produces, in average, less offspring than an infected one. In other words, individual *reproductive* fitness of wild females declines with wild population frequency, and this implies that wild mosquitoes exhibit the so-called frequency-dependent Allee effect at low population densities in the presence of *Wolbachia*-carriers; see [14] and the references therein.

However, there is no record of *Aedes aegypti* being naturally infected by *Wolbachia* [61]. The spread of *Wolbachia* infection among the wild mosquito population can be achieved by large-scale field releases of *Wolbachia*-carriers at some target location. Such carriers of *Wolbachia* are reared under laboratory conditions through the artificial reproduction of mosquito eggs, which are deliberately infected with the *Wolbachia* pathogen taken from other insect species [52]. The international endeavor known as *World Mosquito Program* is currently testing this strategy in the field in 12 countries and has been successful in Australia, Vietnam and Indonesia [1, 23]. In these countries, the introduction of a number of mosquitoes infected with *Wolbachia* in the population triggered an outbreak of *Wolbachia*. The result was the fixation of bacteria in the population, with more than 90 % prevalence with strains *wMel* and *wMelPop* after 10 months since its release. In addition, the release of mosquitoes infected with *Wolbachia* has the advantage of being safe for humans and the environment and economical compared to other control strategies [60], as well as offering protection against subsequent reinvasions with wild mosquitoes from another location.

Recently, Campo-Duarte *et al* [14] have proposed a concise model that accounts for all properties mentioned above. Since only female mosquitoes are responsible for transmission of dengue and other vector-borne infections (male mosquitoes do not bite people), the model takes into consideration only

female populations of mosquitoes. In the deduction of this model, it was fairly supposed that the number of living male mosquitoes is proportional to the number of living female mosquitoes since the mosquito sex ratio at birth is about $1 : 1$ [48]. Under this assumption and at higher frequencies of *Wolbachia*-carrying insects, an average wild female has more chances to encounter with a *Wolbachia*-infected male and to produce inviable eggs, while an average wild male has more chances to mate with a *Wolbachia*-carrying female and to produce *Wolbachia*-infected viable offspring (cf. Table 1).

The model by Campo-Duarte *et al* [14] consists of a set of two nonlinear ordinary differential equations. It was constructed with the aim of proposing a method for population replacement in finite time. The technique in [14] was based on optimal control theory, i.e., the introduction of a control variable to simulate an external, periodical intervention that ensures extinction of wild mosquitoes and survival of *Wolbachia*-infected individuals with minimum duration and costs of implementation; see also [11, 10, 12, 15]. Here, in turn, we complement those previous results by examining the actual basin of attraction of the desired equilibrium state. Concretely, we study how the stable manifold that forms the basin boundary of interest changes under parameter variation. To achieve this, we combine analytical tools from dynamical systems and geometric singular perturbation theory with numerical continuation methods for boundary value problems implemented in Auto [22]. This allows us to present a strategy to get the desired population replacement with a minimum amount of released infected individuals by choosing an appropriate combination of initial conditions and model parameter values. While other works have identified the stable manifold of a saddle equilibrium as the key boundary set to study [36, 47, 83], this is the first time (as far as we know) that this separatrix is analyzed and fully described as the model parameters vary to define a release strategy aiming to minimize this threshold.

We are also interested to investigate a spatially extended version of the model by Campo-Duarte *et al* [14], which takes the form of a set of reaction-diffusion equations. In this extension, we study how the natural dynamics may drive the system into the desired population replacement of mosquitoes across their spatial habitat. This kind of solutions, for instance, may be found as traveling waves [73, 55] that settle into spatially homogeneous steady states corresponding to *Wolbachia* invasion. Spatiotemporal spread of dengue and *Aedes aegypti* mosquitoes as traveling fronts has been the subject of several studies in recent years [17, 51, 71, 72, 81]. Typically, the mathematical analysis involves the reduction of the reaction-diffusion equations into a system of ordinary differential equations in which one searches for heteroclinic orbits; see [35, 50, 55, 77, 80] for instance. However, the problem of obtaining heteroclinic orbits and associated global (un)stable manifolds is a challenging task. With the exception of a few concrete examples (see, e.g., [66]), in general, there are no analytical expressions for homoclinic orbits or nonlocal normal forms. Hence, it is frequent to make use of reductions to Poincaré maps in suitable cross sections or numerical techniques to obtain them; see [71, 81] as examples of this kind of analysis in the context of *Aedes Aegypti* dispersal. Today, homoclinic and heteroclinic orbits can readily be computed and continued with software packages like Auto (with its extension HomCont [16]) and Matcont [20] with high accuracy. In addition, one can locate homoclinic and heteroclinic connections as intersections of global invariant manifolds. This can be achieved by direct computation and inspection of the manifolds [4, 5] or by setting additional techniques such as Lin's method [43]. While one-dimensional invariant manifolds can be approximated using straightforward integration from a given initial condition, the computation of higher-dimensional manifolds of equilibria and periodic orbits requires advanced numerical techniques; see for example [3, 31, 33, 41, 42]. Moreover, while some works have dealt with traveling waves associated with three-dimensional vector fields in population models [49, 71, 81], our problem involves a four-dimensional phase space. This task emerges as a major challenge. To this aim we develop new methods to calculate two and three-dimensional (un)stable invariant objects in a four-dimensional dynamical system. Moreover, we will draw on ingenious visualization techniques —rooted in topological representations of the relevant 3D manifolds and intersections with suitable 3D cross sections— so that useful information can be extracted from these global objects. This is truly uncharted territory in applied dynamical systems. As

far as we know, only very few works have attempted to obtain (up to) two-dimensional manifolds in four dimensional vector fields [32, 58, 74]. With this strategy we find the traveling wave solutions identifying each of them as a specific heteroclinic orbit in the four-dimensional phase space, as well as giving suitable conditions on the propagation speed. In particular, we find uncountably many heteroclinic connections between stationary states (each associated with a wave front exhibiting the desired population replacement), as intersections of global invariant manifolds in the 4D phase space.

This paper is organized as follows. The original model is presented in section 2, and analyzed from the point of view of invariant manifolds and geometric singular perturbation in section 3. We start the study of the spatio-temporal model in section 4 with a local analysis and continue further with the global objects in section 5. The computation and visualization of 3D manifolds associated with traveling fronts is presented in section 6. Section 7 contains a brief summary of the main results and an outline of current and future work. Finally, the appendix presents the mathematical analysis based on geometric singular perturbations that leads to the results in section 3.3.

2. The original model. Let us briefly describe the model proposed by Campo-Duarte *et al.* [14]. Suppose that the population of *Aedes aegypti* females present in each day $t \geq 0$ in some target locality consists of two groups, namely, wild $F(t)$ and *Wolbachia*-carrying $W(t)$ mosquitoes. Both groups compete for the same food resources and breeding sites available in the target locality, as well as for mating opportunities. The evolution of both groups obeys the following population dynamics:

$$\text{(1a)} \qquad \frac{dF}{dt} = \left[\Psi_F - \frac{R_F}{K_F}(F+W) \right] \left(\frac{F}{K_0} - 1 \right) F - \delta_F F,$$

$$\text{(1b)} \qquad \frac{dW}{dt} = \left[\Psi_W - \frac{R_W}{K_W}(F+W) \right] W - \delta_W W.$$

In the equations (1), subindexes "F" and "W" mark the parameters related to wild and *Wolbachia*-carrying mosquitoes, respectively. Namely, $\Psi_{\{F,W\}} > 0$ stand for the natural birth rates of adult female mosquitoes in the absence of density dependence and $\delta_{\{F,W\}} > 0$ denote their natural mortality rates. Therefore, $R_{\{F,W\}} = \Psi_{\{F,W\}} - \delta_{\{F,W\}} > 0$ expresses the intrinsic growth rates of each mosquito group. Equation (1b) states that *Wolbachia*-carrying mosquitoes W exhibit logistic growth with carrying capacity K_W, which is altered by their competition with wild coevals for the same food resources and breeding sites. On the other hand, wild mosquitoes F compete with *Wolbachia*-carrying coevals not only for food resources and breeding sites (cf. terms inside square brackets in (1)), but also for mating opportunities leading to successful reproduction. The latter is modeled by the critical depensation term $\left(\frac{F}{K_0} - 1 \right)$ in the recruitment part of (1a). This term was introduced to mimic the Allee effect exhibited by wild mosquitoes at low densities that significantly affects their reproductive success. In effect, wild female mosquitoes F have "almost" logistic growth when $F > K_0$. However, the recruitment term in (1a) results negative when $F < K_0$, meaning that the population of wild female mosquitoes declines towards extinction. At low densities of wild females ($F < K_0$), wild males also become scarce and they may experience difficulties in finding each other for mating and posterior successful reproduction. In this situation, the probability of cross-matings (i.e., between uninfected females and infected males or vice versa) increases and, therefore, either inviable or *Wolbachia*-infected eggs are produced (see Table 1). It is worth pointing out that the recruitment part of (1b) does not comprise the depensation term, because *Wolbachia*-carrying females are able to produce viable and *Wolbachia*-carrying offspring after mating with either infected or uninfected males.

Since the *wMelPop* strain of *Wolbachia* reduces the individual fitness of *Aedes aegypti* mosquitoes [23, 40, 52, 53, 62, 63], this outcome is reflected by the following relationships imposed on the parameters related to both mosquito groups:

$$\text{(2)} \qquad \Psi_W < \Psi_F, \qquad \delta_W > \delta_F, \qquad R_W < R_F, \qquad K_W < K_F.$$
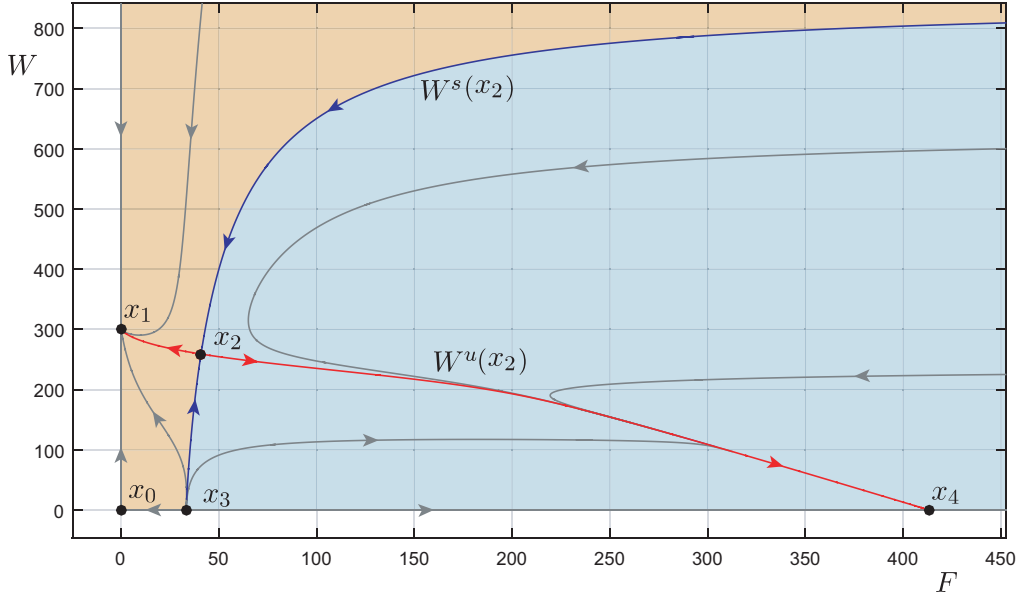
FIG. 1. *Phase portrait of* (1). *The stable* $W^s(x_2)$ *and unstable* $W^u(x_2)$ *manifolds of the equilibrium* x_2 *are represented by blue- and red-colored curves, respectively. The basin of attraction of* x_1 *is the orange region and the basin of attraction of* x_4 *is the light blue area. Parameter values are those in Table 2.*

The first three conditions in (2) basically state that wild females are more fertile and live longer than their coevals infected with *Wolbachia*, while the last relationship indicates that *Wolbachia* infection reduces the insect density in the steady state [21].

Campo-Duarte *et al* [14] have shown that auxiliary parameters K_0 and K_F included in (1a) are tightly related with two important quantities —namely, K_b and K_*— which express, respectively, the minimum viable population size of wild mosquitoes (closely associated with the Allee effect) and the carrying capacity of wild mosquito population (the saturation constant). Furthermore, K_b and K_* can be calculated using the parameters $\Psi_F, \delta_F, K_0,$ and K_F of (1a):

$$(3) \qquad K_b = \frac{R_F K_0 + \Psi_F K_F - \sqrt{\Delta}}{2R_F}, \qquad K_* = \frac{R_F K_0 + \Psi_F K_F + \sqrt{\Delta}}{2R_F},$$

with

$$(4) \qquad \Delta = (K_F - K_0)\Psi_F^2 - 2K_0(K_F + K_0)\Psi_F \delta_F + K_0(4K_F + K_0)\delta_F^2 \geq 0.$$

The meaning of K_b is rather straightforward: in the absence of infected mosquitoes, the population of wild mosquitoes grows ($\dot{F} > 0$) when $F(t) > K_b$ and declines ($\dot{F} < 0$) when $F(t) < K_b$. It was also shown in [14] that under conditions (2), we have

$$(5) \qquad 0 < K_0 < K_b < K_W < K_F < K_*.$$

Campo-Duarte *et al.* [14] showed that the bi-dimensional competitive system (1) has five equilibrium points, namely

$$(6) \qquad x_0 = (0,0), \quad x_1 = (0, K_W), \quad x_2 = (F_c, W_c), \quad x_3 = (K_b, 0), \quad x_4 = (K_*, 0),$$

where the coordinates of K_b and K_* are given by (3) while F_c and W_c are defined by the following

expressions

$$(7) \qquad F_c = \frac{K_0\Big(\Psi_F(K_F - K_W) + \delta_F(K_F + K_W)\Big)}{\Psi_F(K_F - K_W) + \delta_F K_W}, \qquad W_c = K_W - F_c.$$

For realistic parameter values in (1), there are two saddle points (x_0 and x_2), one nodal repeller (x_3), and two nodal attractors (x_1 and x_4). Figure 1 displays the phase plane of system (1) and one can see that the saddle equilibria represent, respectively, eventual extinction of both mosquito groups (x_0) and their unstable coexistence (x_2). The stable manifold $W^s(x_2)$ of strictly positive equilibrium x_2 separates the basins of attraction of x_1 and x_4, which account for eventual extinction of one mosquito population and long term persistence of another, respectively. This outcome perfectly fits the context of the principle of competitive exclusion, according to which only one group of mosquitoes should ultimately survive and persist in the environment.

It is worth pointing out that Figure 1 was plotted using a set of parameters that satisfy the relationships (2) and (5). The underlying numerical values are provided in Table 2 and will be used successively in other sections of this paper.

Parameter	Ψ_F	Ψ_W	δ_F	δ_W	K_0	K_F	K_W
Value	0.32667	0.21333	0.03333	0.06666	30	374	300
Range	$0.29 - 0.38$	$0.18 - 0.25$	$1/42 - 1/8$	$1/21 - 1/4$			

TABLE 2

Representative parameter values for model (1), borrowed from [14].

2.1. Local stability analysis. The Jacobian matrix of (1) at an equilibrium, say (x, y), is given by

$$(8) \qquad J(x, y) = \begin{pmatrix} \frac{K_0 R_F y - \delta_F K_0 K_F - K_0 K_F \Psi_F - 3R_F x^2 + 2x(K_F Pf + K_0 R_F - R_F y)}{K_0 K_F} & \frac{R_F x(K_0 - x)}{K_0 K_F} \\ -\frac{R_W y}{K_W} & \frac{R_W(K_W - x - 2y)}{K_W} \end{pmatrix}.$$

While the eigenvalues of (8) at x_2 are hard to obtain in a closed, analytical form, Campo-Duarte *et al.* [14] have established numerically that x_2 is a saddle for allowed parameter values. In the case of the other equilibrium points, the local stability persists under parameter variation within the ranges of Table 2 and satisfying (2)-(5). This (new) formal result —which is the start of our expansion on the analysis in [14]— is a consequence of Hartman-Grobman theorem [30, 46, 69, 70] and is obtained from direct computation of the eigenvalues of (8) at each equilibrium.

Let us denote the eigenvalues of an equilibrium x_i by λ_i^k where $k = 1, 2$ and $i = 0, \ldots, 4$. The eigenvalues of x_0 are $\lambda_0^1 = -\Psi_F - \delta_F < 0$ and $\lambda_0^2 = \Psi_W - \delta_W > 0$. The eigenvalues of x_1 are $\lambda_1^1 = (\Psi_F - \delta_F)\left(\frac{K_W}{K_F} - \frac{\Psi_F + \delta_F}{\Psi_F - \delta_F}\right) < 0$, and $\lambda_1^2 = -(\Psi_W - \delta_W) < 0$. Hence, x_0 and x_1 are always saddle and attracting node, respectively. On the other hand, the eigenvalues of x_3 are

$$\lambda_3^1 = \frac{\sqrt{\Delta}\Big((K_0 + K_F)\Psi_F - \delta_F K_0 - \sqrt{\Delta}\Big)}{2K_0 K_F(\Psi_F - \delta_F)},$$

$$\lambda_3^2 = \frac{\Big((2K_W - 2K_0)(\Psi_F - \delta_F) + \sqrt{\Delta} - K_F \Psi_F\Big)(\Psi_W - \delta_W)}{2K_W(\Psi_F - \delta_F)};$$

and the eigenvalues of x_4 are

$$\lambda_4^1 = \frac{\sqrt{\Delta}\left(-(K_0 + K_F)\Psi_F + \delta_F K_0 - \sqrt{\Delta}\right)}{2K_0 K_F(\Psi_F - \delta_F)},$$

$$\lambda_4^2 = \frac{-\left((2K_W - K_0)(\Psi_F - \delta_F) + \sqrt{\Delta} + K_F\Psi_F\right)(\Psi_W - \delta_W)}{2K_W(\Psi_F - \delta_F)};$$

where Δ is as in (4). After some algebraic work, it is easy to see that $\lambda_3^1 = \lambda_4^1 = 0$ if and only if $\Delta = 0$. Since $\Psi_F > \delta_F$, then for any choice of the form $(\Psi_F, \delta_F) = (u, ru)$, with $0 < r < 1$ and $u > 0$, we have

$$\Delta = \left((K_F - K_0)^2 - 2K_0(K_F + K_0)r + K_0(4K_F + K_0)r^2\right)u^2 = 0$$

if and only if $2K_0 - K_F \geq 0$, which is not satisfied for parameter values within the range in Table 2. Since $r \in \,]0, 1[$ and $u > 0$ are arbitrary, it follows that the sign of $\Delta > 0$ —and, hence, that of λ_3^1 and λ_4^1— is constant for every realistic parameter value. Straightforward evaluation gives $\lambda_3^1 > 0$ and $\lambda_4^1 < 0$. On the other hand, it is easy to check that $\lambda_4^2 < 0$. Hence, x_4 is an attractor.

Moving on to the eigenvalue λ_3^2 of x_3, we have $\lambda_3^2 = 0$ if

$$\left((K_F + K_W)\delta_F + (K_F - K_W)\Psi_F\right)(K_0 - K_W) + K_F K_W \delta_F = 0.$$

If $K_F K_W - (K_F + K_W)(K_W - K_0) \neq 0$ then $\lambda_3^2 = 0$ along the line $\delta_F = a\Psi_F$ in the (Ψ_F, δ_F)-plane where

$$a = \frac{(K_F - K_W)(K_W - K_0)}{K_F K_W - (K_F + K_W)(K_W - K_0)}.$$

If $K_0 < \frac{K_W^2}{K_F + K_W}$ (as is the actual case for parameters in Table 2) then $a < 0$ and, hence, $\lambda_3^2 > 0$. This completes the analysis of eigenvalues and the local stability of equilibria for the realistic parameter values given by Table 2 and conditions (2)-(5).

On the other hand, let us momentarily allow K_F, K_W and K_0 to vary beyond the conditions imposed by Table 2 such that $K_0 > \frac{K_W^2}{K_F + K_W}$. Then if $K_F < 2(K_W - K_0)$ the slope a satisfies $0 < a < 1$. It follows that the line $\delta_F = a\Psi_F$ lies within the realistic regime defined by (2)-(5). In such case, condition $\lambda_3^2 = 0$ —or equivalently $\delta_F = a\Psi_F$— determines a transcritical bifurcation where x_3 collides and interchanges stability with x_2. (This result agrees with a closer look at the coordinates of x_2 and x_3). For $\delta_F < a\Psi_F$, the equilibrium x_2 becomes negative and x_3 turns into a saddle. This configuration and associated stability persists if $K_0 > \frac{K_W^2}{K_F + K_W}$ and $K_F > 2(K_W - K_0)$ where the slope $a > 1$ and, hence, $\delta_F < a\Psi_F$ for every realistic (Ψ_F, δ_F) satisfying (2)-(5).

3. A strategy to attain full population replacement. Figure 1 shows the stable manifold $W^s(x_2)$ of x_2 acting as a separatrix of the basins of attraction $\mathcal{B}(x_1)$ and $\mathcal{B}(x_4)$. Since long term replacement of wild mosquitoes by infected ones occurs at the equilibrium x_1, any control strategy should aim to drive an initial population beyond the threshold defined by $W^s(x_2)$ and into $\mathcal{B}(x_1)$. Let us consider an initial scenario in which the totality of mosquitoes are of wild type (F). Without loss of generality, assume that the system has reached the stable equilibrium state at $x_4 = (K_*, 0)$, where K_* is given in (3); see the phase portrait in Figure 2. Let $W_0 > 0$ be the amount of *Wolbachia*-infected mosquitoes introduced in the system in an instantaneous release. Then the state of the system shifts to the point (K_*, W_0) in the interior of the first quadrant. Such an external introduction will be successful if $(K_*, W_0) \in \mathcal{B}(x_1)$, i.e., if $W_0 > w^s$, where w^s is the W-coordinate of the point $(K_*, w^s) \in W^s(x_2)$. Furthermore, the lesser w^s is, the fewer infected individuals W_0 must be introduced. The following questions arise: How does the quantity w^s change under parameter variations? In particular which combination of parameters allow w^s to decrease?
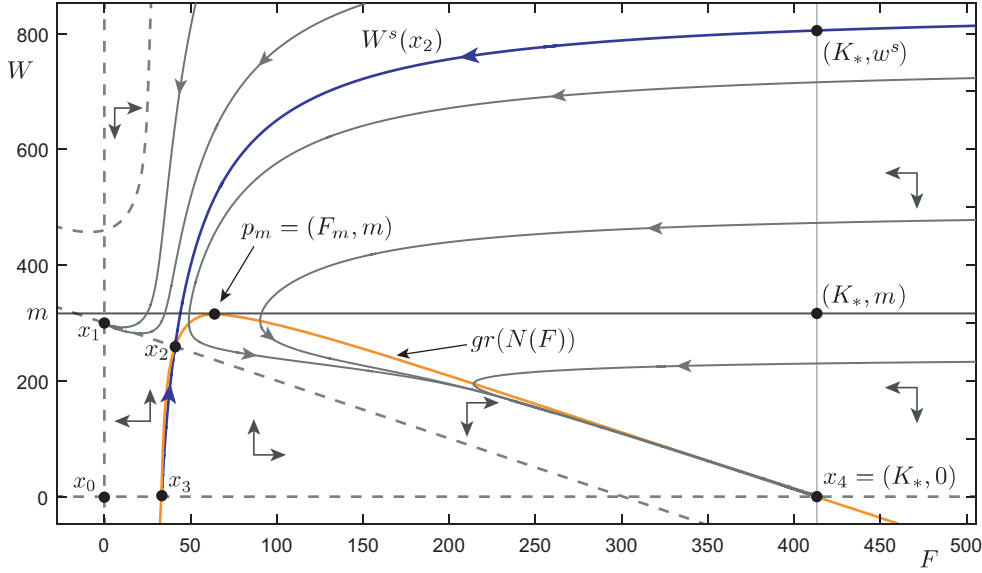
FIG. 2. *A necessary condition for the point (K_*, w^s) to be in $W^s(x_2)$ is that $w^s > m$ where m is the maximum value of the function $W = N(F)$ (plotted as an orange curve). The other nullclines of* (1) *are shown as gray dashed curves. Parameter values are those in Table* 2.

Notice that the stable manifold $W^s(x_2)$ may change its relative position if the point x_2 varies its coordinates. From (6) and (7) we know that the coordinates of the coexistence equilibrium $x_2 = (F_c, W_c)$ do not depend explicitly on the *Wolbachia*-distinctive parameters Ψ_W and δ_W. However, we have

$$\frac{\partial W_c}{\partial \Psi_F} = \frac{\delta_F K_0 K_F (K_F - K_W)}{(\delta_F K_W + (K_F - K_W)\Psi_F)^2} > 0, \quad \frac{\partial W_c}{\partial \delta_F} = -\frac{K_0 K_F (K_F - K_W)}{(\delta_F K_W + (K_F - K_W)\Psi_F)^2} < 0.$$

Therefore, the W-coordinate of x_2 is an increasing function of Ψ_F and decreases with δ_F. Analogously, we have $\frac{\partial F_c}{\partial \Psi_F} = -\frac{\partial W_c}{\partial \Psi_F} < 0$ and $\frac{\partial F_c}{\partial \delta_F} = -\frac{\partial W_c}{\partial \delta_F} > 0$. So the F-coordinate of x_2 is decreasing with Ψ_F and increasing with δ_F. In spite of the point x_2 depending monotonously on Ψ_F and δ_F, we will see in this section that the actual coordinate w^s varies in a nonlinear way with respect to Ψ_F, δ_F, and $R_W = \Psi_W - \delta_W$.

3.1. A lower bound for w^s. In Figure 2 the nullclines of (1) are shown as discontinuous gray curves. The exception is the (orange) curve

$$(9) \qquad\qquad W = N(F) := -F + K_F + \left(\frac{\delta_F}{\Psi_F - \delta_F}\right)\frac{(F - 2K_0)K_F}{F - K_0},$$

which is branch of the F-nullcline. By observing the orientation of the vector field (1) in Figure 2 (illustrated as horizontal and vertical arrows separated by the nullclines), it is easy to see that a necessary condition for the point (K_*, w^s) to be in $W^s(x_2)$ is that $w^s > m$ where m is the maximum value of $W = N(F)$. Otherwise, the orbit through a point (K_*, W_0) with $W_0 < m$ will have an orbit in the basin $\mathcal{B}(x_4)$. The coordinates of the point $p_m = (F_m, m)$ in the graph of $N(F)$ can be found by straightforward calculus: The function $N(F)$ attains its maximum value when

$$(10) \qquad\qquad F = F_m := K_0 + \sqrt{\frac{K_F K_0 \delta_F}{\Psi_F - \delta_F}},$$
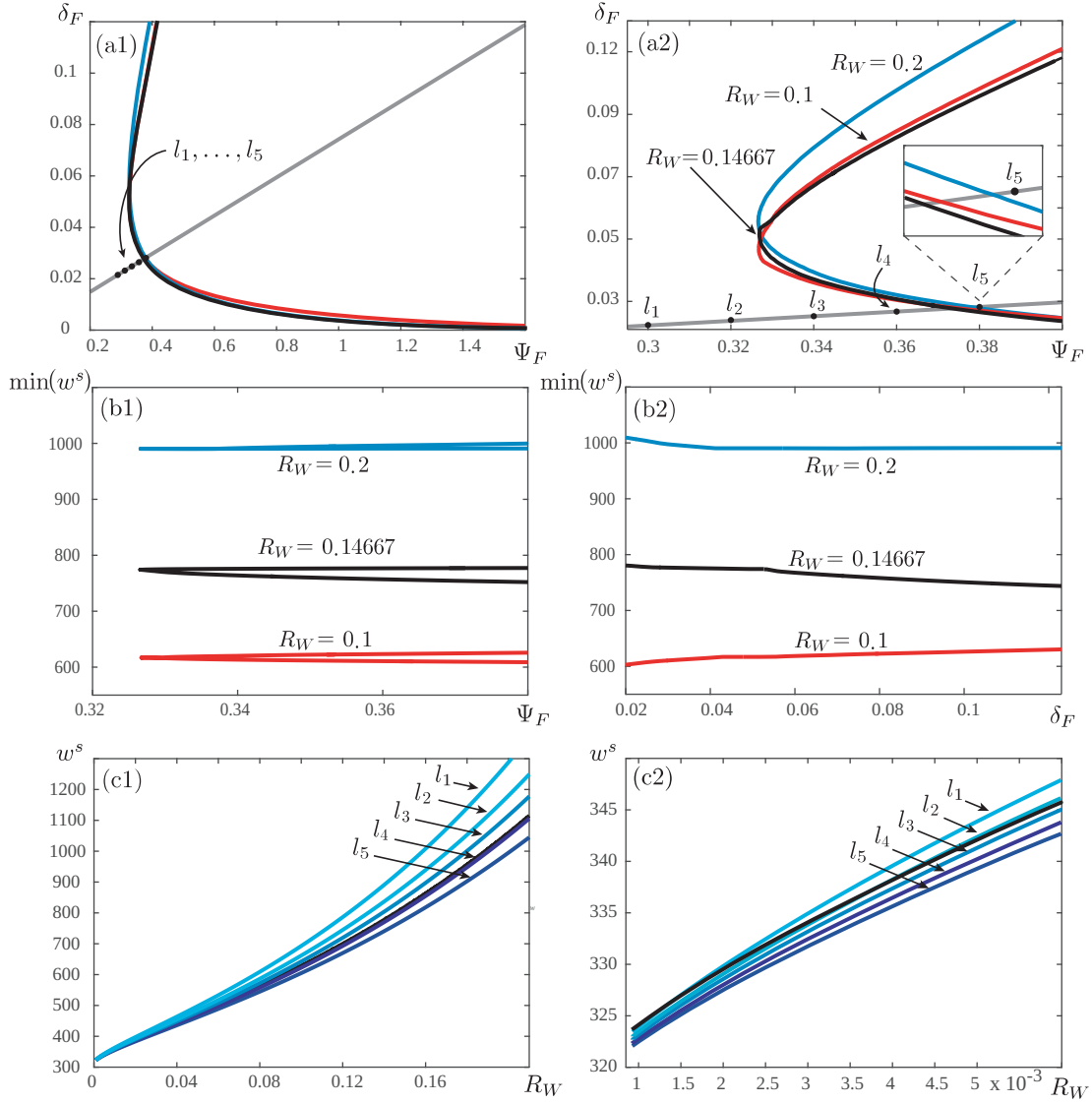
FIG. 3. *The dependence of the threshold value w^s with respect to parameters. Panels (a1)-(a2) show two-parameter curves of minima for w^s in the (Ψ_F, δ_F)-plane for different values of R_W fixed. Also shown is the line L along which m is minimized. The corresponding minimum values of w^s are shown in panels (b1)-(b2). Panels (c1)-(c2) show that w^s is an increasing function of R_W.*

where we obtain:

$$
(11) \qquad m = N(F_m) = \frac{-(\Psi_F - \delta_F)K_0 + \Psi_F K_F - 2\sqrt{\delta_F K_0 K_F(\Psi_F - \delta_F)}}{\Psi_F - \delta_F}.
$$

If we consider (11) as a function $m(\Psi_F, \delta_F)$ of (Ψ_F, δ_F), we have that m reaches its minimum value if and only if $(\Psi_F, \delta_F) \in L$, where

$$
(12) \qquad L = \left\{ (\Psi_F, \delta_F) \in \mathbb{R}_+^2 \mid \delta_F = \frac{K_0}{K_0 + K_F}\Psi_F \right\}.
$$

Hence we obtain

(13) $\inf(w^s) > \min\left(m(\Psi_F, \delta_F)\right) = m|_L = K_F - 2K_0,$

where $K_F - 2K_0 = 314$ according to Table 2.

3.2. Continuation of w^s. Relation (13) defines a lower bound for the threshold w^s, but our analysis has yet to reveal how w^s can approach this bound. In general it is not possible to find the global stable manifold $W^s(x_2)$ in a closed formula. This encumbers to find an analytical expression for w^s. Thus, here we carry out numerical continuation on w^s in terms of the relevant parameters to obtain the minimum values of w^s.

As a first step, we calculate a segment of the upper branch of $W^s(x_2)$ as a solution of a two-point boundary value problem implemented and solved in AUTO. One of these boundary conditions is defined along the stable eigenvector of x_2 at a small distance $\epsilon = 10^{-5}$ from x_2 —a standard procedure to approximate a one-dimensional manifold by continuation [2, 4, 5, 18, 19]. The second boundary condition is located at the vertical line defined by $F = K_*$. In this way, the computed orbit segment represents a piece of $W^s(x_2)$ whose right-hand endpoint $(K_*, w^s) \in W^s(x_2)$ gives away the unknown coordinate w^s. Once the desired segment of $W^s(x_2)$ is obtained, we continue this solution in terms of w^s (which is now a dummy parameter) and δ_F until a fold is detected with respect to w^s. This fold point represents a minimum value of w^s. Finally, we follow this fold point in both δ_F and Ψ_F to trace out a two-parameter curve of minima for w^s.

Figure 3(a1) shows three of these curves in the (Ψ_F, δ_F)-plane computed for fixed values of R_W; also shown is the line L defined by (12). Panel (a2) shows an enlargement of the same elements in the realistic zone. The corresponding minimum values of w^s are shown in panels (b1) (with respect to Ψ_F) and (b2) (with respect to δ_F). Near the point labelled as $l_5 \in L$, each of the three curves of $\min(w^s)$ intersects the line L that minimizes the value of m; see the inlet in Figure 3(a2). Hence, in this region, for given R_W fixed, from (13) one may expect lower values of $\min(w^s)$ as a function of (Ψ_F, δ_F). (In particular, notice that the values of (Ψ_F, δ_F) in this small region are in agreement with the ranges in Table 2 as the ratio $\frac{\Psi_F}{\delta_F} \sim 10$.) However, panels (b1) and (b2) reveal that, for every R_W fixed, fluctuations of $\min(w^s)$ as a function of Ψ_F and δ_F are not very pronounced. On the other hand, in spite of the curves in panels (a1)-(a2) being qualitatively similar, the results in panels (b1)-(b2) show that the possible minima for w^s may indeed have large differences depending on the choice of R_W. More precisely, the more R_W decreases the lower the minima for w^s are. In order to illustrate this dependence, Figure 3(c1) shows the variation of w^s with respect to R_W, with an enlargement for small values of R_W in panel (c2); the values of (Ψ_F, δ_F) are fixed and correspond to selected points $l_1, \ldots, l_5$ in the line L shown in panels (a1)-(a2). It is clear from panels (c1)-(c2) that w^s is an increasing function of R_W. Furthermore, in agreement with the minimizing curves in panels (a1)-(a2), for a given R_W, the closer the values of (Ψ_F, δ_F) are to those that minimize w^s, the lower the values of w^s are in panels (c1)-(c2).

3.3. Slow-fast dynamics. On a first glance, Figures 3(c1) and (c2) suggest that one may seek to adapt infected mosquitoes in a laboratory environment so that parameters Ψ_W and/or δ_W vary to decrease R_W and, hence, w^s. If we define $\epsilon = \frac{R_W}{K_W}$ in (1), we have the typical value $\epsilon \approx 4.89 \times 10^{-4}$ from Table 2. This motivates us to investigate the dynamics for low values of ϵ, which implies that system (1) has an explicit timescales separation. This way we can apply results from Geometric Singular Perturbation Theory for slow-fast systems [26, 39, 45, 34]. While this theory involves the study of the singular limit $\epsilon \to 0$ —an unrealistic case in terms of our model—, it will provide us, in the process, with a valuable understanding of the dynamics for small but strictly positive ϵ. We state here the main results and leave the details for the Appendix.

For $\epsilon > 0$ small we can express (1) in the following equivalent forms describing the dynamics on
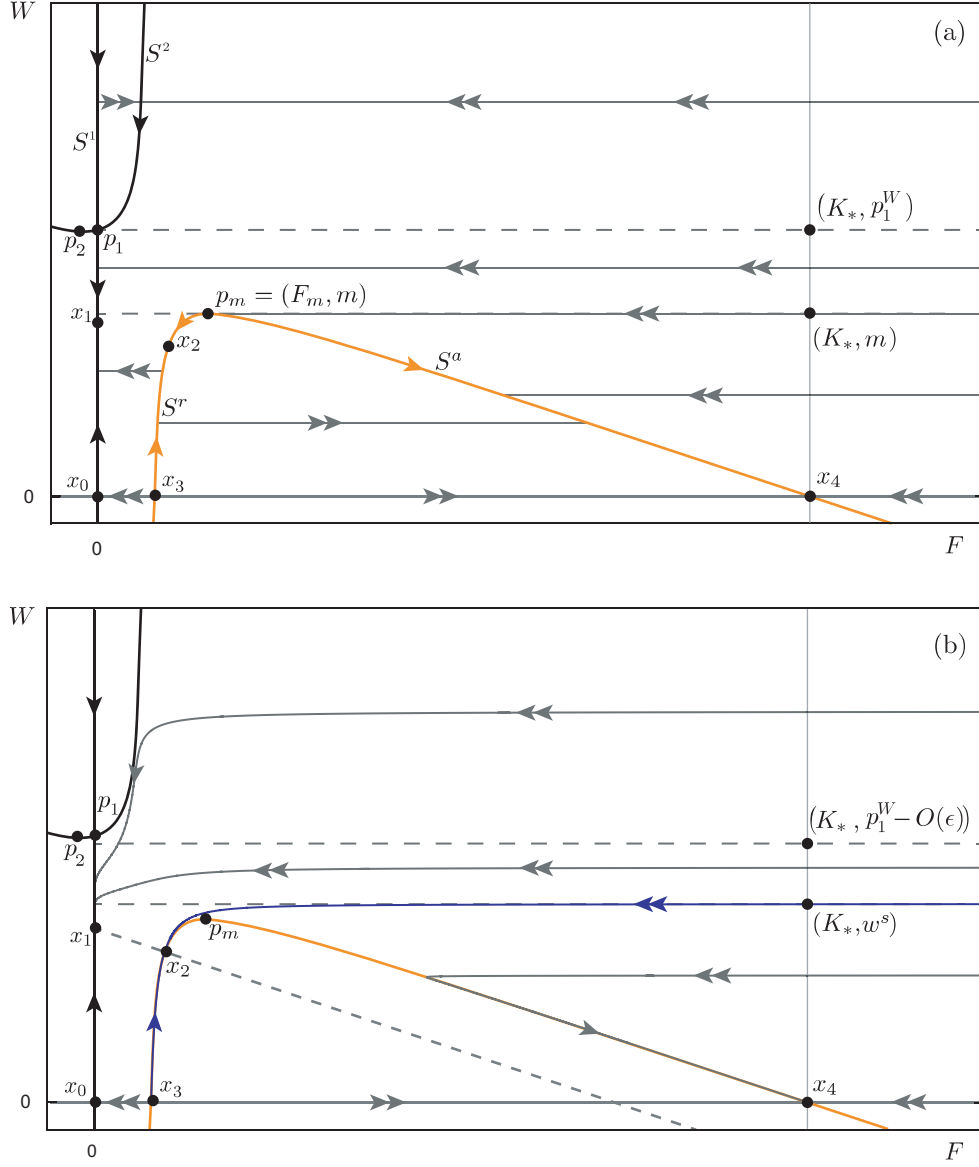
FIG. 4. *The combined sketch of the slow and fast dynamics of (1) for $\epsilon = 0$ (a) and $\epsilon > 0$ (b) in the case that $\delta_F > \frac{K_0}{K_0 + K_F} \Psi_F$. In panel (a) if the initial condition W_0 is within the range $m < W_0 < p_1^W$ the solution is a horizontal line which converges on the fast dynamics towards the attracting sheet of the critical manifold S^1. In turn, in panel (b), if $w^s < W_0 < p_1^W - O(\epsilon)$, the trajectory has a very fast transient for an $O(\epsilon)$-time approaching the axis $\{F = 0\}$, followed by a longer period of time (of order $O(1)$) at a distance $O(\epsilon)$-close to the axis $\{F = 0\}$ before converging to x_1.*

the fast and slow time scale, respectively:

$$
(14) \qquad \begin{cases} F' &= Fh(F,W), \\ W' &= \epsilon\left[K_W W - (F + W)W\right], \end{cases}
$$

or

$$(15) \qquad \begin{cases} \epsilon \dot{F} &= Fh(F,W), \\ \dot{W} &= K_W W - (F+W)W. \end{cases}$$

where $h(F,W) = \left[\Psi_F - \frac{R_F}{K_F}(F+W) \right] \left(\frac{F}{K_0} - 1 \right) - \delta_F$. In this formulation, F evolves as the fast variable and W as the slow one. For ease of explanation, it is convenient to consider first the case where $\delta_F > \frac{K_0}{K_0+K_F}\Psi_F$, i.e., the point (Ψ_F, δ_F) is above the line L defined by (12). A combined phase plane of the slow and fast orbits of (14)–(15) in the singular limit $\epsilon \to 0$ is shown in Figure 4(a). For (14)–(15) the critical manifold, that is, the switch between slow and fast motion, is given by $S = S^1 \cup \{h(F,W) = 0\}$. The curve S is composed by the axis $S^1 = \{F = 0\}$ and the hyperbola $h(F,W) = 0$. This hyperbola has two branches, one of which corresponds to the curve $\{W = N(F)\}$ defined in (9) and shown in orange in Figures 4 and 5; the other branch is labeled as S^2 and crosses the axis $\{F = 0\}$ at $p_1 = \left(0, p_1^W\right)$ where

$$(16) \qquad p_1^W = \frac{K_F(\Psi_F + \delta_F)}{\Psi_F - \delta_F}.$$

Our main interest is on the branch of S given by the graph of $N(F)$. This curve is separated by the fold point $p_m = (F_m, m)$ —given by (10) and (11)— into a repelling branch S^r (for $F < F_m$) and an attracting branch S^a (for $F > F_m$). The branch S^r contains the equilibria x_2 and x_3 which are, respectively, stable and unstable along the slow flow. The branch S^a contains the stable equilibrium x_4. An initial condition (F_0, W_0) outside the critical manifold S has a horizontal orbit which evolves in the fast timescale towards an attracting branch of S. As suggested by our strategy at the beginning of this section, we again consider $F_0 = K_*$. In this way, if the initial condition W_0 is within the range $m < W_0 < p_1^W$ (bounded by two dashed lines in Figure 4(a)), the solution is a horizontal line which converges on the fast dynamics towards the attracting sheet of S^1. In turn, if $W_0 < m$ the orbit converges to S^a, and if $W_0 > p_1^w$, then the orbit approaches S^2.

In the singularly perturbed system ($\epsilon > 0$), Fenichel theory [26, 45] guarantees that attracting and repelling branches of S perturb, respectively, to attracting and repelling slow manifolds. In particular, the branches S^a and S^r of S perturb to slow manifolds S_ϵ^a and S_ϵ^r, respectively, away from the fold point p_m. Figure 4(b) shows the dynamics for small $\epsilon > 0$. The slow manifolds S_ϵ^a and S_ϵ^r have the same stability properties of S^a and S^r and are $O(\epsilon)$ close to them (the same properties hold for slow manifolds perturbed from S^1 and S^2). In particular, for $\epsilon > 0$ the equilibrium x_2 persists and keeps its stability as a hyperbolic saddle of the full system. Moreover, the one-dimensional stable manifold $W^s(x_2)$ has a passage through a fast fiber of the system. After $W^s(x_2)$ passes through a neighborhood of the fold point p_m, it lies $O(\epsilon)$ close to S^r, following a repelling slow manifold S_ϵ^r before converging to x_2. The following result states conditions to ensure a direct, fast passage of a solution towards the axis $\{F = 0\}$; see Figure 4(b):

RESULT 1. *Suppose that $\delta_F > \frac{K_0}{K_0+K_F}\Psi_F$ and that conditions* (2) *and* (5) *hold in* (1). *Let w^s be the W-coordinate of the point $(K_*, w^s) \in W^s(x_2)$ where K^* is as in* (3) *and x_2 is the saddle point defined by* (6)–(7). *Consider an initial condition (K^*, W_0) such that $w^s < W_0 < p_1^W - O(\epsilon)$, where p_1^W is as in* (16). *Then for $\epsilon = \frac{R_W}{K_W} > 0$ sufficiently small, the corresponding solution shows:*
  1. *A very fast transient for an $O(\epsilon)$-time approaching the axis $\{F = 0\}$, followed by...*
  2. *A longer period of time (of order $O(1)$) at a distance $O(\epsilon)$-close to the axis $\{F = 0\}$ before converging to x_1.*

Let us now consider the case when $\delta_F < \frac{K_0}{K_0+K_F}\Psi_F$. The main difference with respect to the previous analysis is that S^2 has a regular fold point in the first quadrant at $p_2 = (p_2^F, p_2^W)$ where
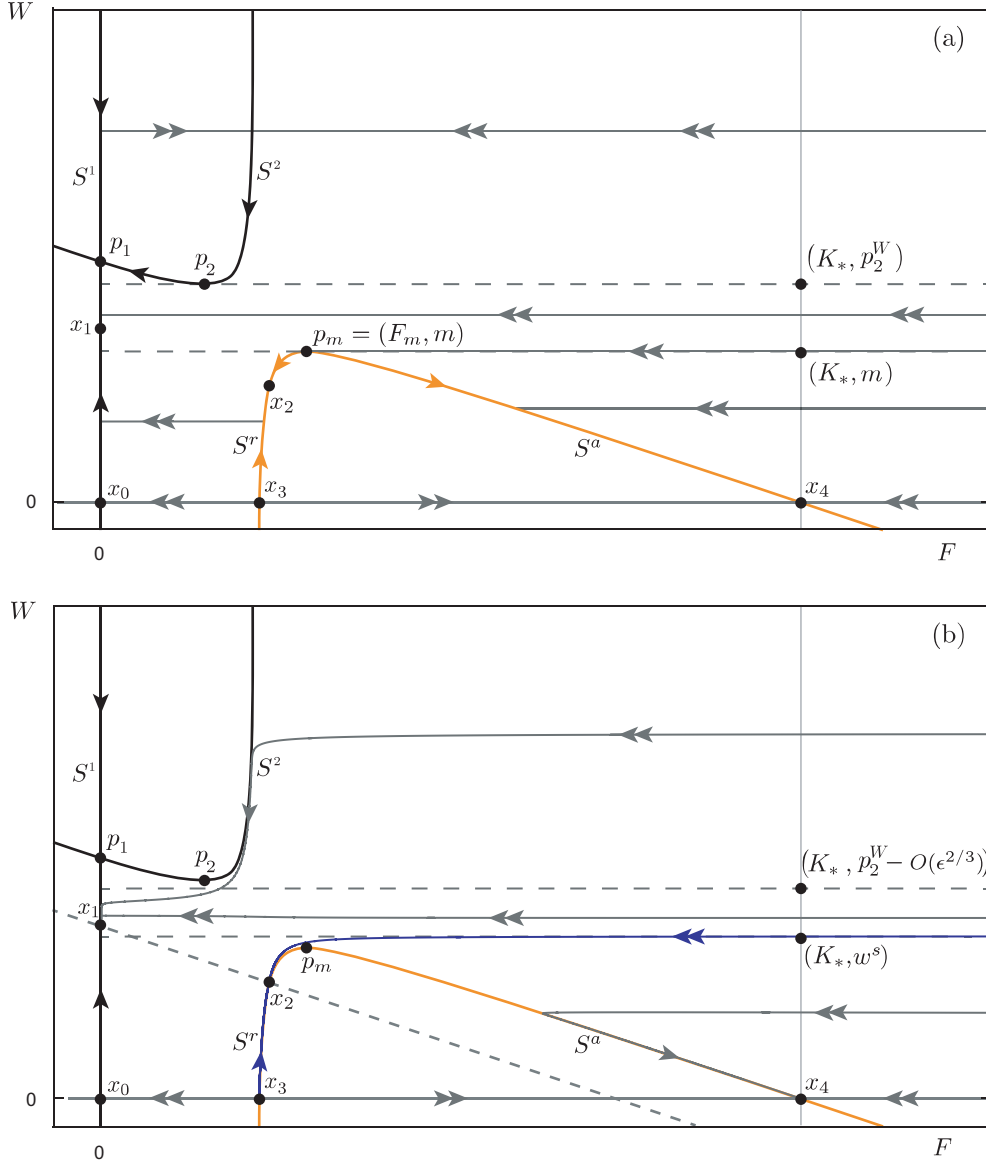
FIG. 5. *The combined sketch of slow and fast dynamics of* (1) *for* $\epsilon = 0$ *(a) and* $\epsilon > 0$ *(b) in the case that* $\delta_F < \frac{K_0}{K_0 + K_F} \Psi_F$. *In panel (a) if the initial condition* W_0 *is within the range* $m < W_0 < p_2^W$ *the solution is a horizontal line which converges on the fast dynamics towards the attracting sheet of the critical manifold* S^1. *In turn, in panel (b), if* $w^s < W_0 < p_2^W - O(\epsilon^{2/3})$, *the trajectory has a very fast transient for an* $O(\epsilon)$-*time approaching the axis* $\{F = 0\}$, *followed by a longer period of time (of order* $O(1)$) *at a distance* $O(\epsilon)$-*close to the axis* $\{F = 0\}$ *before converging to* x_1.

$$p_2^F = K_0 - \sqrt{\frac{K_F K_0 \delta_F}{\Psi_F - \delta_F}} \text{ and}$$

$$(17) \qquad p_2^W = \frac{-(\Psi_F - \delta_F)K_0 + \Psi_F K_F + 2\sqrt{\delta_F K_0 K_F (\Psi_F - \delta_F)}}{\Psi_F - \delta_F}.$$

Under conditions (2) and (5) and the ranges in Table 2, it is easy to check that $p_2^W < p_1^W$. Figure 5(a) shows the combined slow and fast orbits in the singular limit $\epsilon \to 0$ for this case. Hence, if the initial

condition W_0 is within the range $m < W_0 < p_2^W$ (bounded by two dashed lines in Figure 5(a)), the solution converges towards the attracting sheet of S^1 in the fast timescale. In turn, if $W_0 < m$ the orbit converges to S^a, and if $W_0 > p_2^W$, then the orbit approaches the attracting branch of S^2. In the same way as above, attracting and repelling branches of S perturb, respectively, to $O(\epsilon)$-close attracting and repelling slow manifolds away from fold points in the singularly perturbed system ($\epsilon > 0$). Since the two regular folds points p_2 and p_m of S lie in the first quadrant, the two dashed lines in Figure 5(a) must perturb too in order to ensure a fast transition of orbits towards S^1; this is due to the fact that we have slow manifolds extended through the region where the normal hyperbolicity applies. It can be shown [44] that the distance between a slow manifold and a regular fold point has order $O(\epsilon^{2/3})$. Hence, similarly as in the previous case, we have the following result:

RESULT 2. *Suppose that $\delta_F < \frac{K_0}{K_0 + K_F}\Psi_F$ and that conditions (2) and (5) hold in (1). Let w^s be the W-coordinate of the point $(K_*, w^s) \in W^s(x_2)$ where K^* is as in (3) and x_2 is the saddle point defined by (6)–(7). Consider an initial condition (K^*, W_0) such that $w^s < W_0 < p_2^W - O(\epsilon^{2/3})$, where p_2^W is as in (17). Then for $\epsilon = \frac{R_W}{K_W} > 0$ sufficiently small, the corresponding solution shows:*
   1. *A very fast transient for an $O(\epsilon)$-time approaching the axis $\{F = 0\}$, followed by...*
   2. *A longer period of time (of order $O(1)$) at a distance $O(\epsilon)$-close to the axis $\{F = 0\}$ before converging to x_1.*

In both scenarios given by RESULT 1 and RESULT 2, since p_m is a fold point of the critical manifold S, it follows from [44] that the lower threshold w^s can be estimated as $w^s = m + O(\epsilon^{2/3})$, for $\epsilon > 0$ sufficiently small. This gives one a practical way to estimate the range of suitable initial values for W_0. As an illustration, consider typical parameter values in Table 2. Hence $\delta_F - \frac{K_0}{K_0 + K_F}\Psi_F = 0.00907233 > 0$ and we are in the case described by RESULT 1. Moreover, from (11) and (16) we have $m = 315.085$ and $p_1^W = 458.99$. (Notice that m and p_1^W do not depend on the value of $\epsilon = \frac{R_W}{K_W}$.) Therefore, if $0 < \epsilon \ll 1$, the interval $315.085 + O(\epsilon^{2/3}) < W_0 < 458.99 - O(\epsilon)$ defines a range of suitable initial values for W_0 to ensure a very fast transient decay of wild mosquitoes $F(t)$ towards near extinction, followed by a slower convergence of $W(t)$ to the equilibrium value $\lim_{t \to \infty} W(t) = 300$.

4. Traveling waves: Local analysis. In the second half of this work we explore a natural extension to model (1) in which both populations can move over a one-dimensional spatial domain. For this, we consider a reaction-diffusion version given by:

$$(18) \quad \begin{cases} \dfrac{\partial F}{\partial t} = \left[\Psi_F - \dfrac{R_F}{K_F}(F + W)\right]\left(\dfrac{F}{K_0} - 1\right)F - \delta_F F + D_F \dfrac{\partial^2 F}{\partial x^2}, & x \in \mathbb{R}, \quad t > 0, \\[3mm] \dfrac{\partial W}{\partial t} = \left[\Psi_W - \dfrac{R_W}{K_W}(F + W)\right]W - \delta_W W + D_W \dfrac{\partial^2 W}{\partial x^2}, & x \in \mathbb{R}, \quad t > 0, \end{cases}$$

where formally $F = F(x,t)$ and $W = W(x,t)$ are now functions of both position x and time t. In (18) the (non-negative) diffusion coefficients of *Wolbachia*-free *Aedes aegypti* and *Wolbachia*-carrying *Aedes aegypti* are given by the constants D_F and D_W, respectively. The greater these coefficients are the more efficient individuals disperse in space. However, besides the better fitness of *Wolbachia*-free mosquitoes, recent evidence suggests that *Wolbachia*-infected *Aedes Aegypti* mosquitoes show an overall slower spatial spread [67, 76]. Hence we assume that $0 < D_W \leq D_F$.

Here we look for traveling waves of (18) that represent eradication of wild mosquitoes in favour of the *Wolbachia*-infected population. If we consider the time rescaling and change of parameter
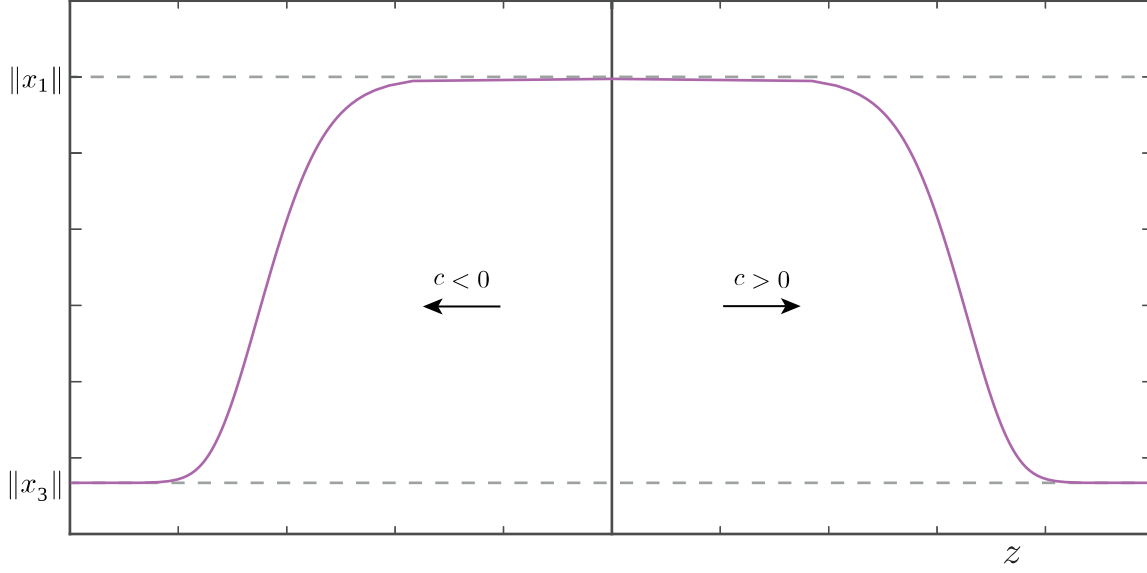
FIG. 6. *Wave front solution of* (18) *joining the steady states* $x_1 = (0, K_W)$ *(as* $z = x - ct \to -\infty$*) to* $x_3 = (K_b, 0)$ *(as* $z \to \infty$*) with speed* $c > 0$*. For* $t > 0$*, this wave front represents a bounded solution that converges towards the full Wolbachia-invasion steady state* x_1*. Transforming each traveling front by* $z \mapsto -z$*,* $c \mapsto -c$*, we also obtain another wave moving in the opposite direction at the same speed.*

$t \mapsto t D_F, D = \frac{D_W}{D_F}$, model (18) is transformed into

$$(19) \quad \begin{cases} \dfrac{\partial F}{\partial t} = \left(\Psi_F - \dfrac{\Psi_F - \delta_F}{K_F}(F + W) \right) \left(\dfrac{F}{K_0} - 1 \right) F - \delta_F F + \dfrac{\partial^2 F}{\partial x^2}, & x \in \mathbb{R}, \quad t > 0, \\[3mm] \dfrac{\partial W}{\partial t} = \dfrac{W}{K_W}(K_W - F - W)(\Psi_W - \delta_W) + D\dfrac{\partial^2 W}{\partial x^2}, & x \in \mathbb{R}, \quad t > 0. \end{cases}$$

Since $D_W \le D_F$ we have $0 < D \le 1$. If we now define the so-called wave variable $z = x - ct$ —where $c > 0$ is the wave speed— and write

$$(20) \qquad F(x, t) = F(x - ct) = F(z), \qquad W(x, t) = W(x - ct) = W(z),$$

system (19) turns into the following set of second order ordinary differential equations

$$(21) \quad \begin{cases} -cF' = \left(\Psi_F - \dfrac{\Psi_F - \delta_F}{K_F}(F + W) \right) \left(\dfrac{F}{K_0} - 1 \right) F - \delta_F F + F'', \\[3mm] -cW' = \dfrac{W}{K_W}(K_W - F - W)(\Psi_W - \delta_W) + DW'', \end{cases}$$

where we denote $u' = du/dz$. System (21) can be expressed equivalently as the four-dimensional vector

field:

$$
(22) \qquad
\begin{cases}
F' = V_F, \\[2mm]
W' = V_W, \\[2mm]
V_F' = \delta_F F - c V_F - \left(\Psi_F - \dfrac{\Psi_F - \delta_F}{K_F}(F+W) \right) \left(\dfrac{F}{K_0} - 1 \right) F, \\[4mm]
V_W' = \dfrac{W}{D K_W}(F + W - K_W)(\Psi_W - \delta_W) - \dfrac{c}{D} V_W,
\end{cases}
$$

which becomes the main object of study in this section and the following one.

The wave variable $z = x - ct$ parameterizes forward orbits of the vector field (22). The equilibrium points of (22) that represent eradication of wild uninfected mosquitoes are $x_0 = (0,0,0,0)$ and $x_1 = (0, K_W, 0, 0)$, where we have kept notation from previous sections for the corresponding equilibria. In particular, x_0 represents the extinction of both populations of mosquitoes, while x_1 symbolizes survival of *Wolbachia*-infected mosquitoes and extinction of wild ones. Figure 6 shows the profile of a wave front starting from x_1 and converging to the *Wolbachia*-free equilibrium $x_3 = (K_b, 0, 0, 0)$, where the coordinate $K_b > 0$ is as in (6) (notice that one also obtains a symmetric wave traveling in the opposite direction at the same speed thanks to the transfomation $z \mapsto -z$, $c \mapsto -c$). This solution corresponds to a heteroclinic orbit in the 4D state space of (22) for which $(F, W) \to (0, K_W)$ as $z \to -\infty$, and $(F, W) \to (K_b, 0)$ as $z \to \infty$. As a consequence, as the wave travels with speed $c > 0$ a transition occurs in (18) from the steady state $(F, W) = (K_b, 0)$ towards $(F, W) = (0, K_W)$ as $t > 0$. Thus the replacement of mosquitoes can be achieved along any positive, bounded solution of (22) for which the associated orbit converges to x_1 as $z \to -\infty$. Hence, our problem is equivalent to investigate selected trajectories of (22) in the unstable manifold of x_1. As a secondary goal, one may also study the unstable manifold of x_0.

As in the previous section, for biological purposes we are interested on $F(z), W(z) \geq 0$ in (22). Let us define the realistic domain in phase space as

$$
\Lambda = \{ (F, W, V_F, V_W) \in \mathbb{R}^4 \mid F, W \geq 0 \}.
$$

4.1. Stability of equilibrium points. System (22) may have up to five equilibrium points in Λ, which are given by $x_0 = (0,0,0,0)$, $x_1 = (0, K_W, 0, 0)$, $x_2 = (F_c, W_c, 0, 0)$, $x_3 = (K_b, 0, 0, 0)$, and $x_4 = (K_*, 0, 0, 0)$, where the coordinates are as in (3) and (7). These equilibrium points are analogous to those in (1). For realistic parameter values in (22) given by Table 2, and conditions (2)-(5), we will prove that the local stability is as follows:

RESULT 3. *The origin x_0 and the coexistence equilibrium x_2 are saddle points with $\dim(W^s) = 3$ and $\dim(W^u) = 1$. The points x_1 and x_4 are also saddles with $\dim(W^s) = \dim(W^u) = 2$. Finally, the equilibrium x_3 is an attractor.*

These results follow directly from Hartman-Grobman's theorem [30] and are obtained below in sections 4.1.1 and 4.1.2. Calculation of eigenvalues of x_2 is a cumbersome task, but direct evaluation of parameters in typical values gives away its stability. In the case of the other equilibria, the stability analysis is facilitated by the restriction of (22) to two invariant planes (presented below) which reduces the dimensionality of the problem. Let us denote the eigenvalues associated with the equilibrium x_k of (22) as λ_i^k, where $i = 1, \ldots, 4$ and $k = 0, \ldots, 4$.

4.1.1. Invariant planes in $\mathbb{R}^4$. System (22) has two invariant planes in the boundary of Λ. These planes are $\Lambda_F := \{ (F, W, V_F, V_W) \in \Lambda \mid W = 0, V_W = 0 \}$ (parameterized by coordinates (F, V_F))

and $\Lambda_W := \{(F, W, V_F, V_W) \in \Lambda \mid F = 0, V_F = 0\}$ (parameterized by coordinates (W, V_W)). The restriction of (22) to the plane Λ_F is given by the following system:

$$(23) \qquad \begin{cases} F' = V_F, \\ V_F' = \delta_F F - cV_F - \left(\Psi_F - \frac{\Psi_F - \delta_F}{K_F}F\right)\left(\frac{F}{K_0} - 1\right)F. \end{cases}$$

The equilibrium points x_0, x_3 and x_4 in (22) defined above are contained in the plane Λ_F and, hence, their (F, V_F) coordinates are equilibria of (23). For simplicity we keep the same notation for $x_0 = (0, 0)$, $x_3 = (K_b, 0)$ and $x_4 = (K_*, 0)$ in (23). The origin x_0 of (23) is a hyperbolic saddle with real eigenvalues $\lambda_1^0 > 0 > \lambda_2^0$ where

$$\lambda_{1,2}^0 = \frac{-c \pm \sqrt{c^2 + 4(\delta_F + \Psi_F)}}{2}.$$

In turn, the eigenvalues of x_3 and x_4 are

$$\lambda_{1,2}^3 = \frac{1}{2}\left(-c \pm \sqrt{c^2 - \frac{\sqrt{\Delta}\left((K_0 + K_F)\Psi_F - \delta_F K_0 - \sqrt{\Delta}\right)}{2K_0 K_F(\Psi_F - \delta_F)}}\right),$$

and

$$\lambda_{1,2}^4 = \frac{1}{2}\left(-c \pm \sqrt{c^2 + \frac{\sqrt{\Delta}\left((K_0 + K_F)\Psi_F - \delta_F K_0 - \sqrt{\Delta}\right)}{2K_0 K_F(\Psi_F - \delta_F)}}\right),$$

respectively, where $\Delta > 0$ is as in (4). From the analysis in section 2.1 we know that $(K_0 + K_F)\Psi_F - \delta_F K_0 - \sqrt{\Delta} > 0$. It follows that in (23) x_3 is an attractor, and x_4 is a hyperbolic saddle.

On the other hand, the restriction of (22) to the plane Λ_W is given by the system

$$(24) \qquad \begin{cases} W' = V_W, \\ V_W' = \frac{W}{DK_W}(W - K_W)(\Psi_W - \delta_W) - \frac{c}{D}V_W. \end{cases}$$

The equilibrium points x_0 and x_1 in (22) are contained in the plane Λ_W and, hence, their (W, V_W) coordinates are equilibria of (24). Once again, we keep the same notation for $x_0 = (0, 0)$ and $x_1 = (K_W, 0)$ in (24). The eigenvalues of x_0 in (24) are

$$(25) \qquad \lambda_{3,4}^0 = \frac{-c \pm \sqrt{c^2 - 4D(\Psi_W - \delta_W)}}{2D}.$$

It follows that x_0 is an attractor of (24). On the other hand, the eigenvalues of x_1 in (24) are $\lambda_{1,2}^1 = \frac{-c \pm \sqrt{c^2 + 4D(\Psi_W - \delta_W)}}{2D}$. Hence, x_1 is a hyperbolic saddle in (24) with $\lambda_1^1 > 0 > \lambda_2^1$.

Remark. If we consider the solutions of (19) with $F \equiv 0$ constant, the problem reduces to the single partial differential equation

$$(26) \qquad \frac{\partial W}{\partial t} = \frac{W}{K_W}(K_W - W)(\Psi_W - \delta_W) + D\frac{\partial^2 W}{\partial x^2}.$$
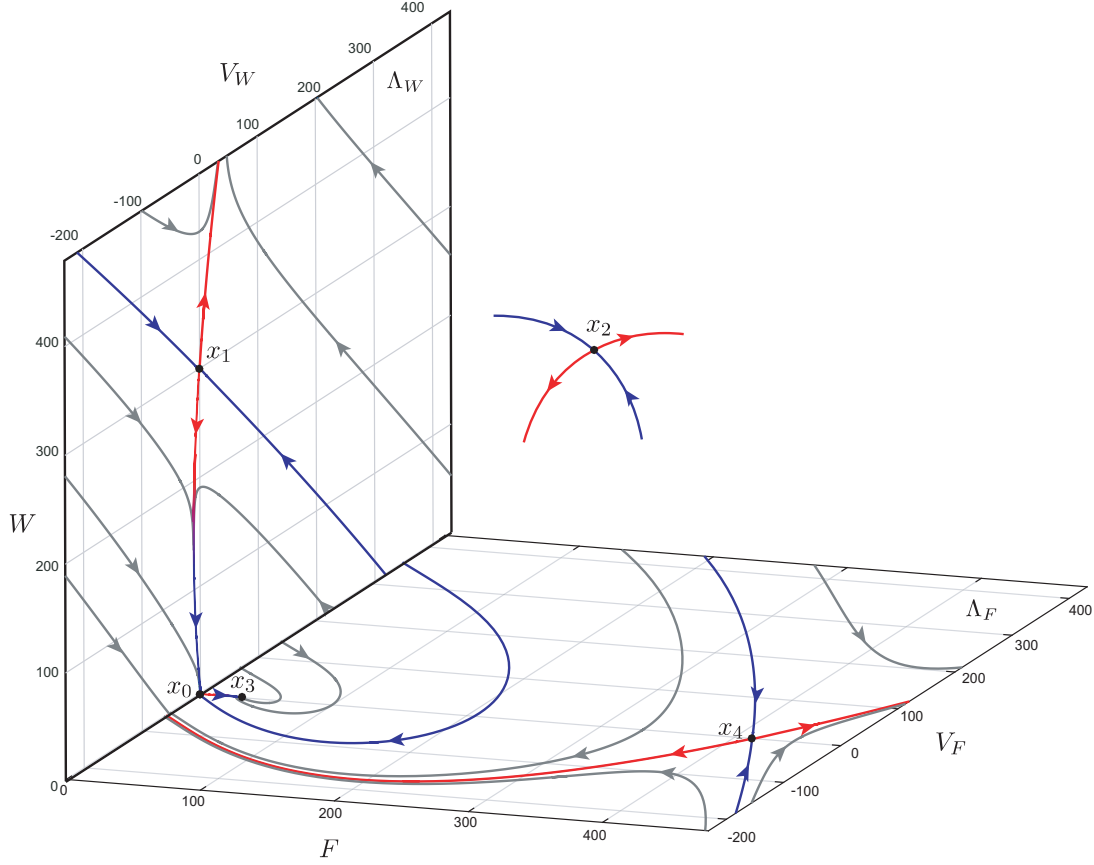
FIG. 7. *Schematic representation of the four-dimensional phase space of* (22) *including the invariant planes* Λ_F *and* Λ_W.

Then searching for traveling wave solutions of (26) in the form (20) leads to the same two-dimensional vector field (24). On the other hand, if one defines a new variable $u = \frac{1}{K_W}W$ and $k = \frac{\Psi_W - \delta_W}{K_W^2}$, then (26) is transformed into the well-known Fisher-Kolmogorov equation [55]:

$$(27) \qquad \frac{\partial u}{\partial t} = ku(1-u) + D\frac{\partial^2 u}{\partial x^2},$$

for which it is known the existence of a wave front $u(z) > 0$ between the steady states $u = k$ and $u = 0$ provided the origin of the associated phase plane is a stable node. It follows from (25) that if $c > 2\sqrt{D(\Psi_W - \delta_W)}$, there is a heteroclinic orbit of (24) contained in the invariant plane Λ_W such that $W(z) > 0$ for every $z \in \mathbb{R}$, $\lim_{z \to -\infty} W(z) = K_W$ and $\lim_{z \to \infty} W(z) = 0$.

4.1.2. Stable and unstable directions from/towards $\mathrm{int}(\Lambda)$**.** The equilibria x_1, x_3 and x_4 of (22) have two remaining eigenvalues associated with incoming and outgoing asymptotic trajectories to or from an invariant plane. In case of x_1 these eigenvalues are

$$(28) \qquad \lambda_{3,4}^1 = -\frac{c}{2} \pm \frac{\sqrt{c^2 K_F + 4\left(\delta_F(K_W + K_F) + \Psi_F(K_F - K_W)\right)}}{2\sqrt{K_F}}.$$

Since $K_F > K_W$, we have $\lambda_3^1 > 0 > \lambda_4^1$. In turn, for x_3 and x_4 we have

$$(29) \qquad \lambda_{3,4}^3 = \frac{1}{2D}\left(-c \pm \sqrt{c^2 - \frac{2D(\Psi_W - \delta_W)\left((2K_W - K_0)(\Psi_F - \delta_F) + \sqrt{\Delta} - K_F\Psi_F\right)}{K_W(\Psi_F - \delta_F)}}\right)$$

and

$$(30) \qquad \lambda_{3,4}^4 = \frac{1}{2D}\left(-c \pm \sqrt{c^2 + \frac{2D(\Psi_W - \delta_W)\left((2K_W - K_0)(\Psi_F - \delta_F) + \sqrt{\Delta} - K_F\Psi_F\right)}{K_W(\Psi_F - \delta_F)}}\right),$$

respectively. From the analysis in section 2.1 we know that $(2K_W - K_0)(\Psi_F - \delta_F) + \sqrt{\Delta} - K_F\Psi_F > 0$. It follows that $\mathrm{Re}(\lambda_{3,4}^3) < 0$ and $\lambda_3^4 > 0 > \lambda_4^4$.

Figure 7 shows a (partial) sketch of the four-dimensional phase space of (22) including the invariant planes Λ_F and Λ_W and the local stability of equilibria.

4.2. Conditions on the propagation speed. Let us recall that our main interest are those trajectories of (22) in $W^u(x_1)$ that converge to other equilibria forming heteroclinic orbits. As a secondary goal we also look at similar orbits in $W^u(x_0)$. Any of these heteroclinic connections must satisfy $F(z) \geq 0$, $W(z) \geq 0$, for all z. Since x_0, x_1, x_3 and x_4 are in the boundary of the domain Λ, this imposes conditions on the unstable eigenvalues of x_1 and x_0 and on the stable eigenvalues of x_3 and x_4 to be real so that the trajectories of interest do not oscillate around $F = 0$ or $W = 0$. In this regard, in section 4.1.1 we already established condition

$$(31) \qquad c > c_1^* = 2\sqrt{D(\Psi_W - \delta_W)}$$

for the heteroclinic connection between x_1 and x_0 in Λ_W. Inequality (31) is the only restriction imposed on c related to x_0 and x_1. Indeed, it follows from the analysis in section 4.1.1 that $W^u(x_0)$ is a one-dimensional unstable manifold contained in the invariant plane Λ_F. The branch of $W^u(x_0)$ in Λ converges to x_3 and satisfies $F(z) > 0$, $W(z) = 0$, for all z; see Figure 7. Moreover, from (28), x_1 has an unstable direction towards $\mathrm{int}(\Lambda)$ associated with the eigenvalue $\lambda_3^1 > 0$, which is real for every $c > 0$.

Furthermore, x_3 has two stable eigenvalues given by (29) associated with trajectories coming from $\mathrm{int}(\Lambda)$. It follows that $\lambda_{3,4}^3 \in \mathbb{R}$ if

$$(32) \qquad c > c_2^* = \sqrt{\frac{2D(\Psi_W - \delta_W)\left((2K_W - K_0)(\Psi_F - \delta_F) + \sqrt{\Delta} - K_F\Psi_F\right)}{K_W(\Psi_F - \delta_F)}}.$$

Finally, from the analyses in sections 4.1.1 and 4.1.2 both stable eigenvalues of x_4 are real for every $c > 0$.

Direct comparison between the minimum wave speeds in (31)-(32) leads to

$$(c_1^*)^2 - (c_2^*)^2 = \frac{2D(\Psi_W - \delta_W)\left((K_0 + K_F)\Psi_F - \delta_F K_0 - \sqrt{\Delta}\right)}{K_W(\Psi_F - \delta_F)} > 0,$$

since $(K_0 + K_F)\Psi_F - \delta_F K_0 - \sqrt{\Delta} > 0$. Therefore, we obtain that the minimum wave speed is $c_{min} = c_1^*$ as in (31). For instance, in terms of parameter values in Table 2, we have $c_{min} = 0.76595D^{1/2}$.
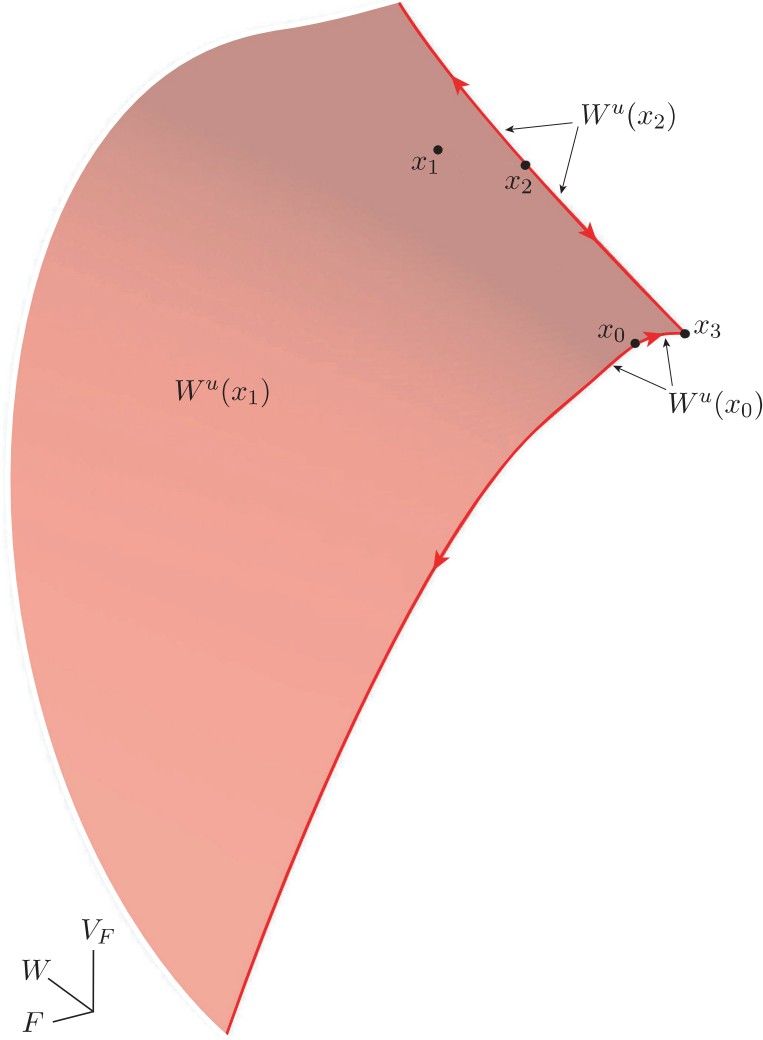
FIG. 8. *A piece of $W^u(x_1)$ projected onto the (F, W, V_F)-coordinates. The manifold $W^u(x_1)$ is bounded by $W^u(x_0)$ and $W^u(x_2)$. Parameter values are as in Table 2, with $D = 0.9$, and $c = 1$.*

5. Traveling waves: Global invariant manifolds and saddle connections. Recall that orbits of (22) that converge to x_1 as $z \to -\infty$ represent traveling wave solutions of (18) that induce full invasion of *Wolbachia*-infected mosquitoes and elimination of wild uninfected individuals. Our focus in this section is, hence, the study of the two-dimensional unstable manifold $W^u(x_1)$ of x_1 in the four-dimensional phase space of (22). Since most of this analysis is of a computational nature —though strongly rooted in dynamical systems theory—, in what follows we fix parameters in those typical values in Table 2. Moreover, we choose the ratio $D = \frac{D_W}{D_F} = 0.9$ in order to account for the lower mobility of infected mosquitoes; see [67, 76]. Accordingly, we also consider $c = 1 > c_{min} \approx 0.726644$.

Figure 8 shows a piece of $W^u(x_1)$ projected onto the (F, W, V_F)-coordinates. This surface was obtained with the method of continuation of orbit segments [3, 41, 42]. In this setting, the global manifold is computed as a family of solutions of a two-point boundary value problem implemented and solved in AUTO; see further details on the computational implementation and other applications
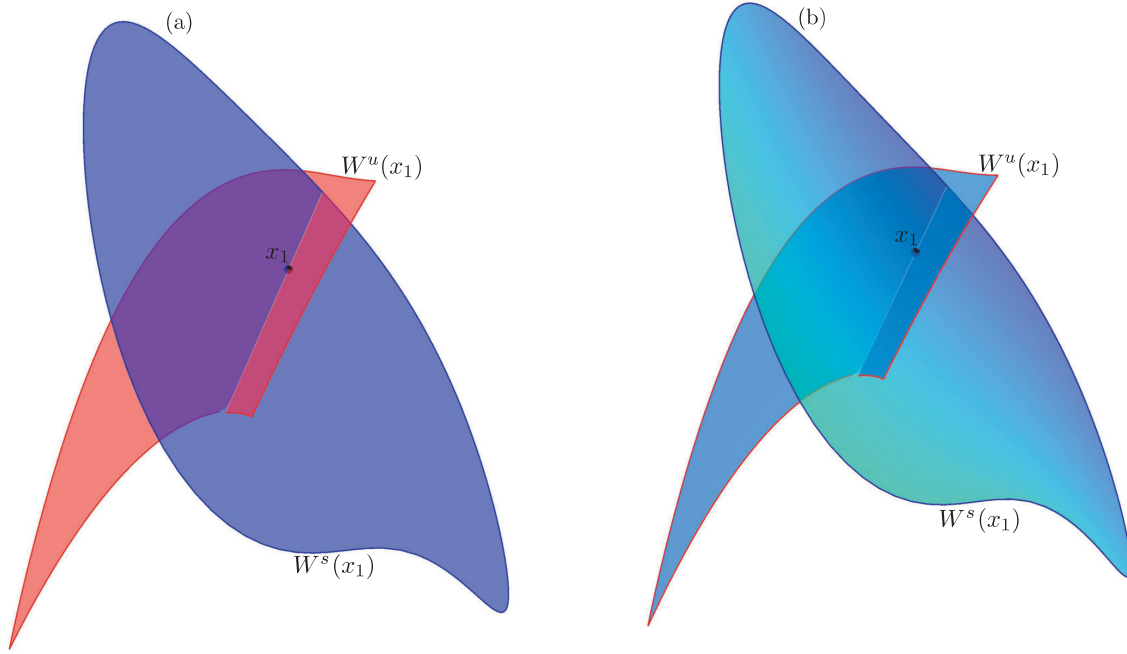
FIG. 9. *The stable manifold $W^s(x_1)$ and unstable manifold $W^u(x_1)$ of (22) in a projection onto the (F, W, V_F)-coordinates. The apparent intersection of manifolds in panel (a) is revealed in panel (b) as an artifact produced by the projection. A color code has been setup for the missing coordinate V_W in panel (b). Along any real intersection colors (and coordinates) should match. Parameter values are as in Figure 8.*

of this algorithm in [2, 4, 31]. The computed piece of $W^u(x_1)$ has two boundaries, namely, the one-dimensional manifolds $W^u(x_0)$ and $W^u(x_2)$. In particular, Figure 8 suggests there are some orbits in $W^u(x_1)$ that converge to one of the equilibria x_0, x_2 and x_3 to form heteroclinic connections.

All heteroclinic (and homoclinic) orbits (if any) come as intersections of stable and unstable manifolds. It is not straightforward, in general, to confirm that any such intersection in the four-dimensional phase space is real and not a visual artifact due to the projection onto a lower-dimensional section. However, one may follow the approach from [58] to check on the apparent intersections of two-dimensional manifolds of (22). Figure 9(a) shows two pieces of the two-dimensional manifolds $W^u(x_1)$ and $W^s(x_1)$ crossing one another along a curve through x_1 in what may be interpreted as an evidence of homoclinic orbits. However, the value of the fourth coordinate V_W is missing in this projection and, hence, Figure 9(a) is not conclusive. The approach from [58] is to plot both manifolds with a color code that depends on the V_W-coordinate. If there is a true intersection between $W^u(x_1)$ and $W^s(x_1)$ there must be a color matching along $W^u(x_1) \cap W^s(x_1)$; otherwise, it is just a ficticious intersection. For instance, Figure 9(b) confirms there is no homoclinic connection to x_1 since colors (and hence the V_W-coordinates) do not match along the intersection. We remark that similar inspections can be done in any other apparent intersections of two-dimensional manifolds. We omit the false ones here to economize space and focus next on the actual intersections.

Figure 10 shows the organization of phase space of (22) in a projection onto the (F, W, V_F) hyperplane. The invariant sets present in Figure 10 are the one-dimensional unstable manifolds $W^u(x_0)$ and $W^u(x_2)$, the two-dimensional manifolds $W^s(x_1)$, $W^u(x_1)$, $W^s(x_4)$ and $W^u(x_4)$, and the strong stable manifolds $W^{ss}(x_0)$ and $W^{ss}(x_2)$. Here blue (resp. red) surfaces represent stable (resp. unstable) manifolds. We also computed approximations of selected pieces of the full three-dimensional
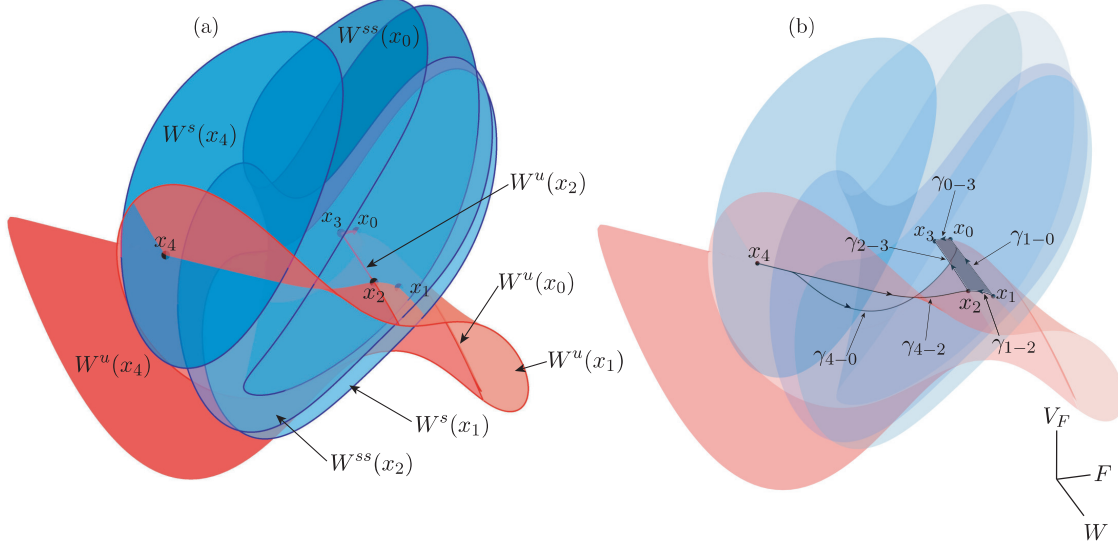
FIG. 10. *Invariant manifolds (and submanifolds) of dimensions one and two of* (22) *in a projection to the three-dimensional* (F, W, V_F)-*hyperspace. Panel (a) shows the surfaces layout in phase space while panel (b) shows the same manifolds in a transparent rendering to reveal the heteroclinic connections. Parameter values are as in Figure* 8.

stable manifolds $W^s(x_0)$ and $W^s(x_2)$ with the method described later in section 6.1; we opted to not show them here for ease of visualization. Panel (a) in Figure 10 is useful to illustrate the convoluted layout of the two-dimensional invariant manifolds. However, it is not yet clear what are the actual intersections of $W^u(x_1)$ (our main object of study) with other manifolds which give rise to hetero-clinic orbits. A closer inspection of the three-dimensional manifolds and the use of a more transparent rendering of surfaces clarifies this question. Panel (b) shows that there are two isolated heteroclinic orbits starting from x_1, labeled as γ_{1-0} and γ_{1-2}. The orbit γ_{1-0} connects x_1 to x_0, while γ_{1-2} starts from x_1 and converges to x_2 as $z \to \infty$. Also shown in Figure 10(b) are the orbits γ_{4-0} and γ_{4-2} connecting x_4 to x_0 and x_2, respectively. In particular, γ_{4-0} and γ_{1-0} are connections contained in the invariant planes Λ_F and Λ_W, respectively; see section 4.1.1. Other connections are also present in Figure 10(b), each connecting x_0 or x_2 to x_3, and labeled as γ_{0-3} and γ_{2-3}, respectively. Notably, the four heteroclinic orbits γ_{1-0}, γ_{1-2}, γ_{0-3} and γ_{2-3} bound a shaded region in $W^u(x_1)$ which consists of orbits of $W^u(x_1)$ that converge to x_3. Hence, it follows that there are uncountably many heteroclinic connections between x_1 and x_3 contained in $W^u(x_1)$.

A sample of the connections from x_1 to other equilibria is illustrated in Figure 11 as time series in the independent variable z (rescaled between 0 and 1). The vertical axis indicates the Euclidean norm of each solution. Each one of these heteroclinic orbits represents a wave front traveling with speed $c > 0$ from a uniformly steady state given by equilibrium x_0, x_2 or x_3 towards x_1. In particular, the continuum of heteroclinic orbits found in $W^u(x_1)$ —represented here by a sample of solutions and denoted collectively as Γ_{1-3}— is bounded by γ_{1-2} and γ_{1-0}. Every solution in the collection Γ_{1-3} corresponds to a possible transition of (18) from a *Wolbachia*-free scenario —represented by equilibrium x_3— towards total population replacement by *Wolbachia*-carriers at x_1 as $t \to \infty$. For instance, Figure 12(a) shows one of such heteroclinic connections $\gamma_{1-3} \subset \Gamma_{1-3}$ in $W^u(x_1)$. If one observes the state variables at three different times $0 < t_0 < t_1 < t_2$, two wave front solutions with speed c —one moving to the left and the other moving to the right— develop in the sequence of
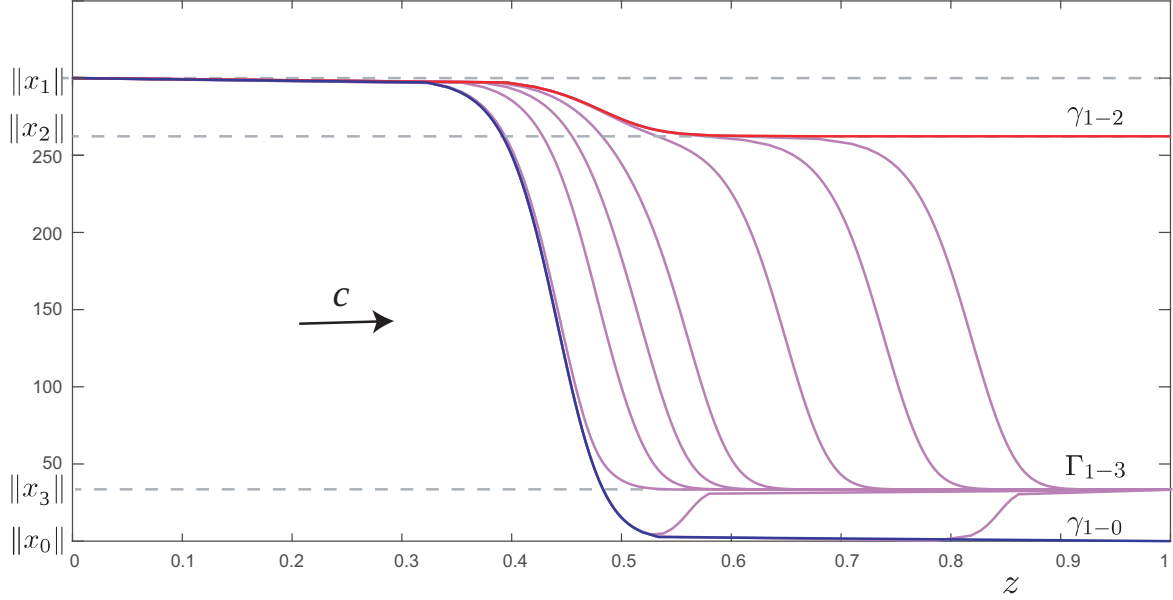
FIG. 11. *Travelling fronts of (18) joining different initial spatially uniform steady states to x_1 ensuring the desired population replacement. The time series γ_{1-2} indicates a front from x_2 to x_1 while γ_{1-0} signals a transition from x_0 to x_1. Moreover, there are uncountably many travelling fronts joining x_3 to x_1, labelled collectively as Γ_{1-3}. All solutions plotted here correspond to actual orbits found in Figure 10. Parameter values are as in Figure 8.*

panels (b)-(d) in Figure 12. It is important to emphasize that all solutions in Γ_{1-3} correspond to different orbits of (22) and, hence, to different wave solutions of (18); that is, one cannot simply obtain one of them from another one by means of translations of the wave variable z. Moreover, in the 4D phase space, orbits in $W^u(x_1)$ in the vicinity of γ_{1-2} and γ_{1-0} spend long transients visiting the neighbourhoods of x_2 and x_0, respectively. As a consequence, one can also distinguish traveling fronts that seem to settle around the steady states x_2 or x_0 for long intervals of z before converging eventually to x_3; see again Figure 11.

The equilibrium x_3 is the only bounded attractor of (22). The basin $\mathcal{B}(x_3)$ of x_3 in the four-dimensional phase space is bounded by the stable manifolds $W^s(x_0)$ and $W^s(x_2)$, which are three-dimensional invariant sets (orbits in the interior of the complement of $\mathcal{B}(x_3) \cup W^s(x_0) \cup W^s(x_1) \cup W^s(x_4)$ simply go to infinity as $z \longrightarrow \infty$). On the other hand, $W^u(x_1)$ is two-dimensional. Hence, the heteroclinic orbits found in section 5 flowing from x_1 towards x_0, x_2 or x_3 represent transverse intersections of invariant manifolds in $\mathbb{R}^4$ [31, 68]. Since, in addition, all the equilibria are hyperbolic, it follows that the continuum of desired traveling waves is robust under small parameter variations.

6. 3D invariant manifolds in the 4D phase space. In this work we did not find any other heteroclinic orbits emerging from x_1 in (22). The purpose of this section is to present the main rationale behind this result. While heteroclinic orbits γ_{1-0}, γ_{1-2}, γ_{0-3}, γ_{2-3}, γ_{4-0} and γ_{4-2} were found by direct computation and inspection of the associated global two-dimensional invariant manifolds (see Figure 10), further connections (if any) with 3D objects have yet to be ruled out. To do so, our approach is based on examination of intersections of the 2D unstable manifold $W^u(x_1)$ with the 3D manifolds $W^s(x_0)$ and $W^s(x_2)$ which act as separatrices in the 4D ambient space. For a better understanding we will illustrate the method of computation and visualization of three-dimensional invariant manifolds in the specific case of $W^s(x_0)$ in (22).
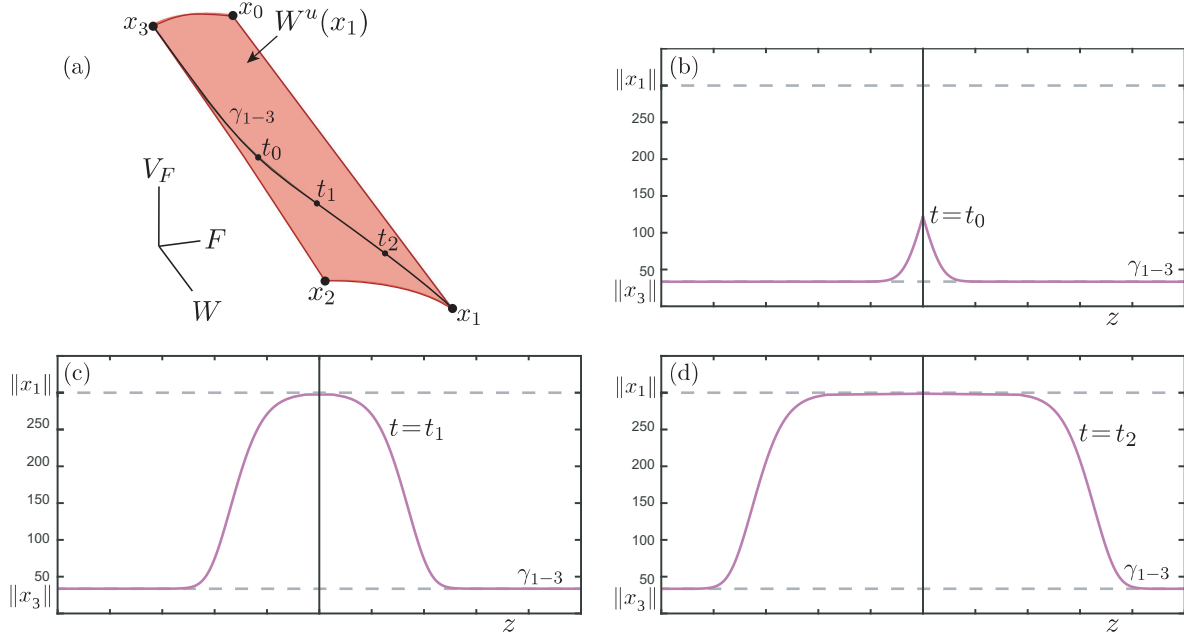
FIG. 12. *System* (22) *may have uncountably many heteroclinic orbits joining x_1 and x_3. This continuum of connections correspond to a family of orbits in $W^u(x_1)$. Panel (a) shows one such connection with distinguished locations at different times $t_0 < t_1 < t_2$. Observing the state variables of* (19) *at these positions, one obtains two wave front solutions with speed c (one moving to the left and the other moving to the right) corresponding to a transition in panels (b)-(c)-(d) towards total population replacement by* Wolbachia-carriers. *Parameter values are as in Figure* 8.

6.1. Computation of 3D manifolds. The general set-up is based on an extension of the scheme built to calculate two-dimensional manifolds via the continuation of orbit segments [3, 41, 42]. Consider a function $\mathbf{u} : [0, 1] \mapsto \mathbb{R}^4$ satisfying the differential equation

$$\text{(33)} \qquad \frac{d}{d\tau}\mathbf{u}(\tau) = Tf(\mathbf{u}(\tau)),$$

where $f(\cdot)$, in our case, stands for (22) and $T > 0$ is the integration time (also known as the "period") of an orbit segment of the vector field f. System (33) is a rescaled version of (22) with a new independent variable $\tau = Tz$. In this way, in (33), the period T appears as an explicit parameter and the actual integration time over an orbit segment is always 1. Geometrically, the function $\mathbf{u}$ represents a unique orbit segment $\{\mathbf{u}(\tau) \in \mathbb{R}^4 \,|\, 0 \leq \tau \leq 1\}$ provided that suitable boundary conditions are posed at one or both end points $\mathbf{u}(0)$ and $\mathbf{u}(1)$.

In order to keep this presentation as general as possible, let $\mathbf{p}$ be a saddle equilibrium of f and suppose the stable eigenvalues of $\mathbf{p}$ are $\lambda_1^s \leq \lambda_2^s < \lambda_3^s < 0$, so that $W^s(\mathbf{p})$ is a three-dimensional manifold (notice this is the actual case for both x_0 and x_2 in (22)). In our case, we take advantage of the Stable Manifold Theorem [30, 46] that states that $W^s(\mathbf{p})$ is tangent to the linear eigenspace $E^s(\mathbf{p})$ at $\mathbf{p}$. We represent $W^s(\mathbf{p})$ as a collection $\mathcal{M}^\theta = \{W_\theta^s\}$ of topological disks parameterised by θ. For each fixed θ a topological disk is obtained as a family of orbit segments $W_\theta^s := \{\mathbf{u}_{\varphi,\theta}(\tau) : \tau \in [0,1]\}_{\varphi,\theta}$ —parameterised by φ— whose endpoints $\mathbf{u}(1)$ lie on a small ellipsoid in the three-dimensional linear eigenspace $E^s(\mathbf{p})$ and are sufficiently close to $\mathbf{p}$. For every fixed θ, the disk W_θ^s is a connected two-dimensional submanifold; hence, the manifold $W^s(\mathbf{p})$ of dimension three is foliated by the collection
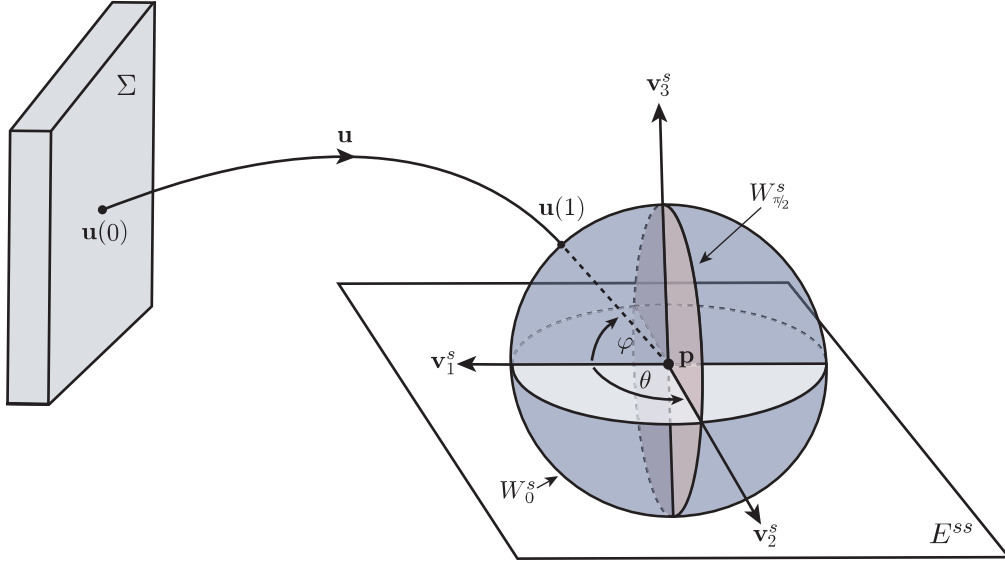
FIG. 13. *Sketch of the ellipsoid around* $\mathbf{p}$ *defined by* (34) *in a projection to the three-dimensional eigenspace* $E^s(\mathbf{p})$. *In particular, the strong stable space* E^{ss} *corresponds to the union of the half planes* $\varphi = 0$ *and* $\varphi = \pi$. *Also shown is the codimension-one submanifold* Σ *projected here as a three-dimensional cross-section.*

$\mathcal{M}^\theta$. For this, we now consider (33) and the boundary condition:

$$(34) \quad \mathbf{u}(1) = \mathbf{p} + \epsilon \left(\cos(\varphi) \left(\cos(\theta) \frac{\mathbf{v}_1^s}{|\lambda_1^s|} + \sin(\theta) \frac{\mathbf{v}_2^s}{|\lambda_2^s|} \right) + \sin(\varphi) \frac{\mathbf{v}_3^s}{|\lambda_3^s|} \right), \quad \theta \in [0, \pi], \quad \varphi \in [0, 2\pi),$$

where $\mathbf{v}_k^s$, $k = 1, 2, 3$, are the (unit) stable eigenvectors associated with the eigenvalues of $\mathbf{p}$, and $\epsilon > 0$ is sufficiently small. The variation of $(\theta, \varphi) \in [0, \pi) \times [0, 2\pi)$ defines a fundamental domain where every approximated trajectory in $W^s(\mathbf{p})$ intersects this ellipsoid exactly once. The BVP (33)–(34) defines a (θ, φ, T)-dependent family of orbit segments. For any fixed $T = T_0$ and $\theta = \theta_0$ we have a uniquely defined invariant disk $W_{\theta_0}^s$ that consists of a φ-family of orbit segments with fixed integration time T_0 parameterised by $\varphi \in [0, 2\pi)$ whose endpoints $\mathbf{u}(1)$ lie on a small ellipse near $\mathbf{p}$; see the sketch in Figure 13 in a projection to the three-dimensional eigenspace $E^s(\mathbf{p})$.

In order to compute this φ-family by continuation in AUTO, we need to specify an initial orbit segment $\mathbf{u}_{\varphi_0} \in W_{\theta_0}^s$ that satisfies (33)–(34) for some fixed $\varphi = \varphi_0 \in [0, 2\pi)$ and $\theta = \theta_0 \in [0, \pi)$. To this end, a possible choice is to consider the constant solution $\mathbf{u}_0 \equiv \mathbf{p} + \epsilon\, \mathbf{v}_1^s / |\lambda_1^s|$ of (33) with $T = 0$ —i.e., a trivial orbit segment—; continuation in T for fixed $\mathbf{u}(1) = \mathbf{u}_0$ up to $T = -T_0$ yields the desired initial orbit segment $\mathbf{u}_{\varphi_0}$ satisfying (33)–(34) for $\theta_0 = 0$ and $\varphi_0 = 0$ (note that this continuation step is effectively integration from $\mathbf{u}(1)$ backwards in time). The collection $W_{\theta_0}^s$ of orbits segments is then obtained by fixing $T = -T_0$ and continuing $\mathbf{u}_{\theta_0}$ in φ over the interval $[0, 2\pi)$. Moreover, by construction, the family W_θ^s lies in an $O(\epsilon^2)$ neighbourhood of $W^s(\mathbf{p})$. The three-dimensional manifold $W^s(\mathbf{p})$ is then seen as the collection $\mathcal{M}^\theta = \{W_\theta^s\}$ of invariant leaves W_θ^s as θ sweeps over the interval $[0, \pi]$.

Note that by imposing $\varphi_0 = 0$ or $\varphi_0 = \pi$, the initial orbit $\mathbf{u}_{\varphi_0}$ (with $T = -T_0$ fixed) lies on the two-dimensional strong stable manifold $W^{ss}(\mathbf{p})$. Hence, one can readily adapt our scheme to obtain this invariant submanifold by fixing $\varphi = \varphi_0 \in \{0, \pi\}$ and continuing $\mathbf{u}_{\varphi_0}$ allowing θ to vary over the interval $[0, 2\pi)$.

Sometimes, it is convenient to restrict the point $\mathbf{u}(0)$. This allows one, for instance, to calculate the intersection set $W^s(\mathbf{p}) \cap \Sigma$ with a codimension-one submanifold $\Sigma = \{\mathbf{x} \in \mathbb{R}^4 : G(\mathbf{x}) = 0\}$, by
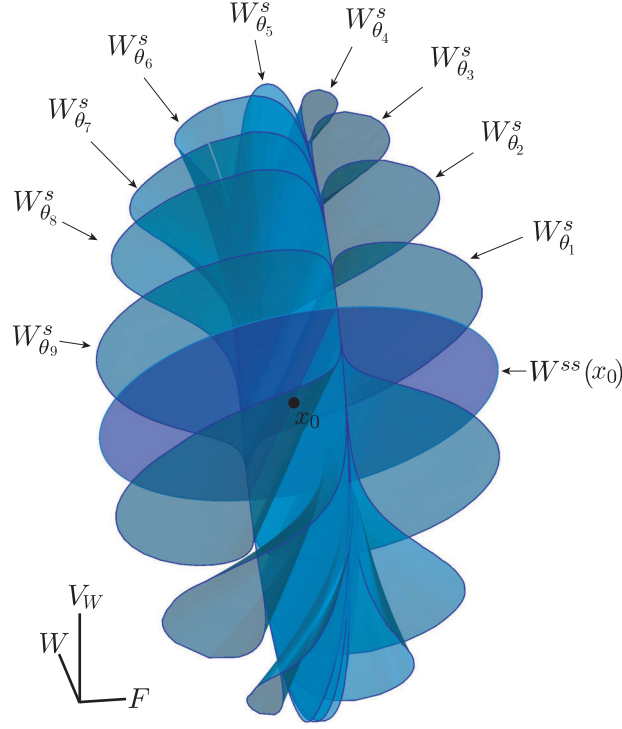
FIG. 14. *Projection of a computed piece of $W^s(x_0)$ onto the (F, W, V_W)-coordinates in* (22). *The three-dimensional manifold is seen as a collection of leaf-shaped invariant disks obtained with the method in section* 6.1. *Parameter values are as in Figure* 8.

imposing the second boundary condition

$$(35) \qquad\qquad\qquad G(\mathbf{u}(0)) = 0.$$

The solutions of (33) with boundary conditions (34) and (35) are trajectories that start on Σ and end in the fundamental domain near the origin. For every fixed θ and φ, this BVP has a locally unique solution with a given value of T, which is now a free parameter. Provided $W^s(\mathbf{p})$ and Σ intersect transversally, points $\mathbf{u}(0)$ in $W^s(\mathbf{p}) \cap \Sigma$ form a codimension two submanifold which is not invariant. We approximate $W^s(\mathbf{p}) \cap \Sigma$ as a two-parameter collection of endpoints $\mathbf{u}(0)$ parameterized by (θ, φ). An initial orbit segment of this BVP can be found by continuation in T of any solution satisfying (34) for some fixed choice of $\varphi = \varphi_0 \in [0, 2\pi)$ and $\theta = \theta_0 \in [0, \pi)$; we monitor the value of $G(\mathbf{u}(0))$ and stop the continuation when condition (35) is satisfied. This starting orbit segment can then be continued as a one-parameter family of solutions of the BVP (33), (34), (35) in the free parameters (φ, T) with $\theta = \theta_0$ fixed, so that the point $\mathbf{u}(0)$ traces out a one-dimensional curve on Σ. An approximation of the two-dimensional set $W^s(\mathbf{p}) \cap \Sigma$ is then obtained as we repeat the process for different values of θ over the interval $[0, \pi)$.

6.2. Visualization of invariant objects in four dimensions. Figure 14 shows a projection of the three-dimensional manifold $W^s(x_0)$ of x_0 onto the (F, W, V_W)-coordinates. The computed piece of $W^s(x_0)$ consists of a collection of invariant disks W^s_θ (rendered as transparent surfaces) obtained with the method described above for a selection of fixed values of $\theta \in [0, \pi)$. The endpoints $\mathbf{u}(0)$ in each disk lie in the three-dimensional sphere

$$(36) \qquad\qquad\qquad \mathbb{S}^3 = \{\mathbf{x} \in \mathbb{R}^4 : \ ||\mathbf{x}|| = r\},$$
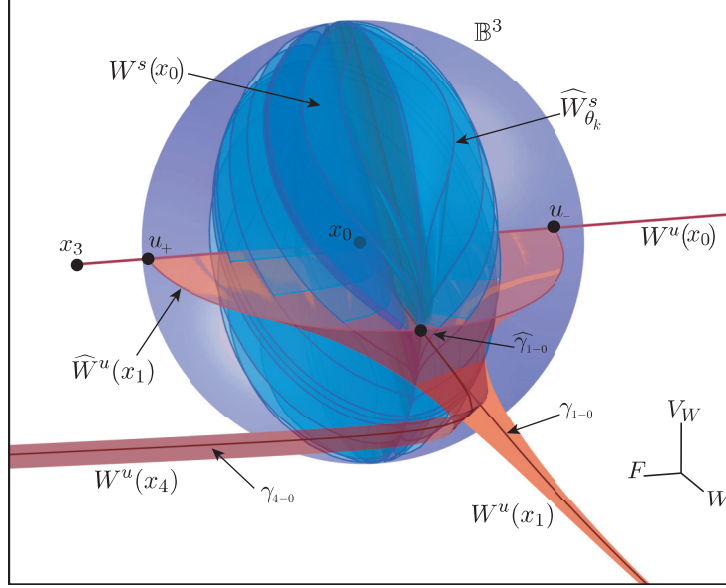
FIG. 15. *The sphere $\mathbb{S}^3$ is projected onto the (F, W, V_W)-coordinates as a solid 3-ball $\mathbb{B}^3$ centered at x_0. The computed piece of $\widehat{W}^s(x_0)$ consists of a collection of (blue) curves $\widehat{W}^s_{\theta_k} := W^s_{\theta_k} \cap \mathbb{S}^3$. Those regions of the selected invariant disks $W^s_{\theta_k}$ located inside the sphere $\mathbb{S}^3$ in $\mathbb{R}^4$ are projected as blue surfaces in $\mathbb{B}^3$. Also shown are the manifolds $W^u(x_1), W^u(x_4)$ and $W^u(x_0)$ and their intersections with $\mathbb{S}^3$ labeled as $\widehat{W}^u(x_1)$, $\widehat{W}^u(x_4)$ and $\widehat{W}^u(x_0) = \{u_+, u_-\}$, respectively. In particular, $\gamma_{1-0} \subset W^u(x_1) \cap W^s(x_0)$ intersects $\mathbb{S}^3$ at the point $\widehat{\gamma}_{1-0}$.*

centered at the origin $x_0 \in \mathbb{R}^4$ with $r = 25$ (not shown in Figure 14). Following the analysis in section 4.1, most orbits within $W^s(x_0)$ approach x_0 along the leading eigendirection defined by $\mathbf{v}^s_3 = (0, \ 0.985217, \ 0, \ -0.171311)$ which is contained in the invariant plane (W, V_W). A manifestation of this fact in the chosen projection is that each of the leaf-shaped disks W^s_θ tends to accumulate on one another in the vicinity of x_0 along the leading eigendirection contained in the plane $F = 0$. The exception is the strong stable manifold $W^{ss}(x_0)$ which is tangent to the linear space spanned by $\mathbf{v}^s_1 = (0.615338, \ 0, \ -0.788263, \ 0)$ and $\mathbf{v}^s_2 = (0, \ -0.729636, \ 0, \ 0.683836)$.

Figure 14 is useful in that it reveals the nature of $W^s(x_0)$ as a topological three-dimensional ball immersed in $\mathbb{R}^4$. The more invariant disks are included in the rendering of $W^s(x_0)$, the better this manifold is approximated as a solid volume foliated by the leaves W^s_θ. However, the subdivision of different basins of attraction by $W^s(x_0)$ and the presence of connecting orbits is yet unclear. Our strategy is to study the intersection of $W^s(x_0)$ and the other invariant manifolds with the 3-sphere $\mathbb{S}^3$ (36) with $r = 25$ (for this choice of radius, the origin x_0 is the only equilibrium in the interior of $\mathbb{S}^3$). This is obtained by considering the boundary condition (35) with

$$G(\mathbf{u}(0)) = u_1^2(0) + u_2^2(0) + u_3^2(0) + u_4^2(0) - r^2.$$

Since $\mathbb{S}^3$ is compact, this representation is very useful to study basins of attraction of the stable objects. In this way, the set $\widehat{W}^s(x_0) := W^s(x_0) \cap \mathbb{S}^3$ is typically a 2D submanifold in the interior of $\mathbb{S}^3$ at all points where the intersection is transversal. Figure 15 shows $\mathbb{S}^3$ and the invariant objects in a projection onto the (F, W, V_W)-hyperplane. Such projection of $\mathbb{S}^3$ corresponds to the (transparent) solid ball $\mathbb{B}^3 = \{(F, W, V_W) \in \mathbb{R}^3 : F^2 + W^2 + V_W^2 \leq r^2\}$ centered at the origin x_0. The computed piece of $\widehat{W}^s(x_0)$ consists of a collection of (blue) curves $\widehat{W}^s_{\theta_k} := W^s_{\theta_k} \cap \mathbb{S}^3$ obtained with the method described above for a selection of fixed values of $\theta_k \in [0, \pi)$. As a visual reference, Figure 15 also displays those regions of the selected invariant disks $W^s_{\theta_k}$ located inside the sphere $\mathbb{S}^3$ in $\mathbb{R}^4$; such
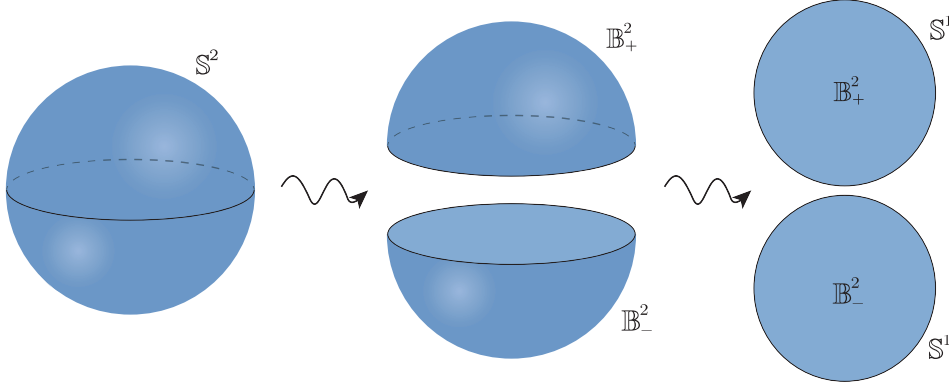
FIG. 16. *An example of dimension reduction to help visualization of the 3-sphere $\mathbb{S}^3$: A 2-sphere $\mathbb{S}^2$ is seen as the union of two topological disks (or hemispheres) $\mathbb{B}^2_+$ and $\mathbb{B}^2_-$ with their common boundary —a circle $\mathbb{S}^1$— corresponding to the equator of $\mathbb{S}^2$.*

projections in Figure 15 correspond to the blue surfaces inside $\mathbb{B}^3$. Notice that, in Figure 15, most of the points in a curve $\widehat{W}^s_{\theta_k}$ are contained in the interior of $\mathbb{B}^3$. In turn, the set $\widehat{W}^u(x_0) := W^u(x_0) \cap \mathbb{S}^3$ consists of two points $\{u_+, u_-\}$. The side of $W^u(x_0)$ that contains u_+ converges to the point x_3, while the other side goes to infinity. On the other hand, the set $\widehat{W}^u(x_1) := W^u(x_1) \cap \mathbb{S}^3$ is a one-dimensional locus in $\mathbb{B}^3$ and contains the point $\widehat{\gamma}_{1-0} := \gamma_{1-0} \cap \mathbb{S}^3$. Either end of the curve $\widehat{W}^u(x_1)$ is bounded by the points u_+ and u_-, respectively. Likewise, the set $\widehat{W}^u(x_4) := W^u(x_4) \cap \mathbb{S}^3$ is also one-dimensional and is located very close to $\widehat{W}^u(x_1)$.

It is important to note that the apparent intersection of $W^u(x_1)$ with a number of leaves $W^s_{\theta_k} \subset W^s(x_0)$ in Figure 15 is a visual trick produced by the projection. Since any real intersection must manifest itself in $\mathbb{S}^3$, our strategy is to investigate the actual intersections of $\widehat{W}^s(x_0)$ and $\widehat{W}^u(x_1)$ directly in $\mathbb{S}^3$. Naturally, this task requires to introduce a visualization approach for objects in $\mathbb{S}^3 \subset \mathbb{R}^4$. Let us first motivate this choice with a brief example in $\mathbb{R}^3$. Let $\mathbb{S}^2 = \{x \in \mathbb{R}^3 : \|x\| = r\}$ be the 2-sphere in $\mathbb{R}^3$ of radius $r > 0$ in Figure 16. Each hemisphere of $\mathbb{S}^2$ is homeomorphic to a disk, i.e., a 2-ball $\mathbb{B}^2$ with a circle $\mathbb{S}^1$ as common boundary. Hence, the sphere $\mathbb{S}^2$ can be topologically seen as the union of two disks $\mathbb{B}^2$ where their boundaries (topological circles $\mathbb{S}^1$) are identified and represent the equator of $\mathbb{S}^2$. Likewise, back in $\mathbb{R}^4$, the sphere $\mathbb{S}^3$ can be decomposed topologically as the union of two 3-balls $\mathbb{B}^3$ (as in upper and lower "hemispheres") where their common boundary is a sphere $\mathbb{S}^2$ representing the "equator" of $\mathbb{S}^3$.

Concretely, let us consider $\mathbb{S}^3$ as the union of the upper ($V_F > 0$) and lower ($V_F < 0$) hemispheres of $\mathbb{S}^3$ where the common boundary corresponds to the equator $V_F = 0$ of $\mathbb{S}^3$ (points in this boundary satisfy $F^2 + W^2 + V_W^2 = r^2$). Let us plot these hemispheres in a three-dimensional space by choosing the projection onto the remaining (F, W, V_W)-coordinates. Figure 17 shows such projections labeled as $\mathbb{B}^3_+$ and $\mathbb{B}^3_-$ for the upper and lower hemispheres, respectively. The boundaries of $\mathbb{B}^3_+$ and $\mathbb{B}^3_-$ —the corresponding spherical shells— are identified and, hence, we name the common boundary $\partial \mathbb{B}^3$. On the other hand, the centers of $\mathbb{B}^3_+$ and $\mathbb{B}^3_-$ correspond to the points $(0, 0, r, 0)$ and $(0, 0, -r, 0)$ in $\mathbb{R}^4$, respectively. The corresponding intersections of $\mathbb{S}^3$ and invariant objects of (22) are also displayed on each hemisphere in Figure 17. The computed piece of $\widehat{W}^s(x_0)$ consists of a collection of (blue) curves $\widehat{W}^s_\theta := W^s_\theta \cap \mathbb{S}^3$ obtained for a selection of fixed values of $\theta \in [0, \pi)$. The more invariant disks are included in the rendering of $W^s(x_0)$, the better $\widehat{W}^s(x_0)$ is approximated as a surface foliated by the curves $\widehat{W}^s_\theta$ in each hemisphere; compare to Figure 15. Indeed, each part of $\widehat{W}^s(x_0)$ contained in either hemisphere $\mathbb{B}^3_+$ or $\mathbb{B}^3_-$ is a topological disk whose boundary consists of a simple closed curve that lies
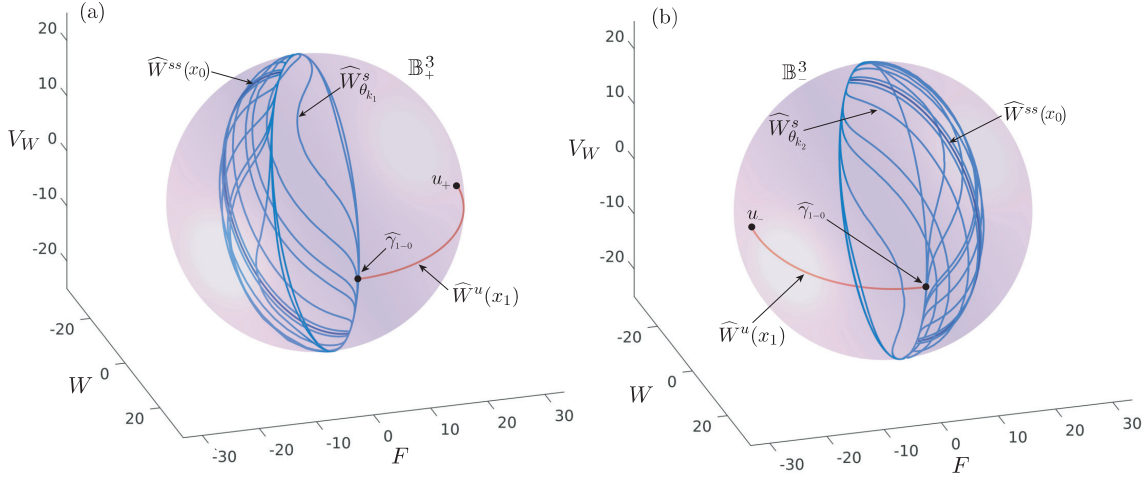
FIG. 17. *The intersections of $\mathbb{S}^3$ and invariant objects of (22) is best described by examining each hemisphere of $\mathbb{S}^3$ labeled as $\mathbb{B}^3_+$ and $\mathbb{B}^3_-$, respectively. A collection of (blue) curves $\widehat{W}^s_\theta$ approximates $\widehat{W}^s(x_0)$. Variation of θ in $[0,\pi)$ gives rise to a surface representing the computed piece of $\widehat{W}^s(x_0)$. The one-dimensional set $\widehat{W}^u(x_1)$ is present in both hemispheres, each part bounded by a point in $\widehat{W}^u(x_0) = \{u_+, u_-\}$ and by the heteroclinic point $\widehat{\gamma}_{1-0}$.*

in $\partial\mathbb{B}^3$.

In Figure 17 the set $\widehat{W}^u(x_1)$ consists of two loci, one in each hemisphere. One end of each locus is bounded by a point in $\widehat{W}^u(x_0)$; u_+ on the side in $\mathbb{B}^3_+$, and u_- in $\mathbb{B}^3_-$. Both parts of $\widehat{W}^u(x_1)$ are joined together in $\partial\mathbb{B}^3$ at $\widehat{\gamma}_{1-0} \subset \widehat{W}^u(x_1) \cap \widehat{W}^s(x_0)$ (visible in both hemispheres). Moreover, the point $\widehat{\gamma}_{1-0}$ lies in the boundary circle $\widehat{W}^s(x_0) \cap \partial\mathbb{B}^3$. Since $\widehat{W}^u(x_1) \cap \widehat{W}^s(x_0)$ consists of a single point, it follows that γ_{1-0} is the only heteroclinic connection between x_1 and x_0 in the full four-dimensional phase space.

Actual intersections of invariant manifolds in $\mathbb{R}^4$ emerge with clarity thanks to the approach of Figure 17. However, it is still unclear how $W^s(x_0)$ is separating different basins of attraction. Hence, the final step in our visualization strategy is to examine the relevant objects in each hemisphere in Figure 17 in cross sections $\Sigma_v = \{(F, W, V_F, V_W) \in \mathbb{R}^4 : V_W = v\}$ for different levels of the variable V_W. Namely, for each ball $\mathbb{B}^3_\pm$ and each fixed $V_W = v$ with $-r < v < r$, the set $\mathbb{B}^3_\pm \cap \Sigma_v$ is homeomorphic to a topological disk. In local coordinates (F, W) each disk $\mathbb{B}^3_\pm \cap \Sigma_v$ is given by $F^2 + W^2 \leq r^2 - v^2$. The center of this disk corresponds to the point $(F, W, V_F, V_W) = \left(0, 0, \pm\sqrt{r^2 - v^2}, v\right) \in \mathbb{S}^3$, where the sign $\pm$ is determined by the choice of hemisphere. On the other hand, points in the boundary of this disk correspond to points in the equator $\{V_F = 0\}$ of $\mathbb{S}^3$. The result is shown in Figure 18: Panels (a) and (b) show the intersection sets of Σ_v with the hemispheres $\mathbb{B}^3_+$ and $\mathbb{B}^3_-$, respectively, for $v = -2.5$. Panels (c) and (d) show the same respective sets for $v = 15$, while panels (e)-(f) correspond to $v = 24$. For each v the set $\widetilde{W}(x_0) := \widehat{W}^s(x_0) \cap \Sigma_v$ is now a one-dimensional closed curve separated into two segments, one on each hemisphere, and connected at the boundary circle. This representation unfolds the nature of $\widetilde{W}(x_0)$ —and, hence, of $W^s(x_0)$— as a separatrix: The shaded region labeled $\widetilde{\mathcal{B}}(x_3)$ corresponds to points in the basin of attraction $\mathcal{B}(x_3)$ of x_3; in turn, the white region is the basin of attraction of infinity. In particular, for $v = -2,5$ in panels (a) and (b), the set $\widetilde{W}^s(x_1) := \widehat{W}^u(x_1) \cap \Sigma_v$ corresponds to two points, one on each basin and both very close to the boundary circle. Additional cross sections for other values of v show the same distribution of the set $\widetilde{W}^s(x_1)$; since the resulting pictures are essentially the same as those in panels (a)-(b), we do not show them here. As a consequence, a typical trajectory in $W^u(x_1)$ that intersects $\mathbb{S}^3$ either converges to x_3
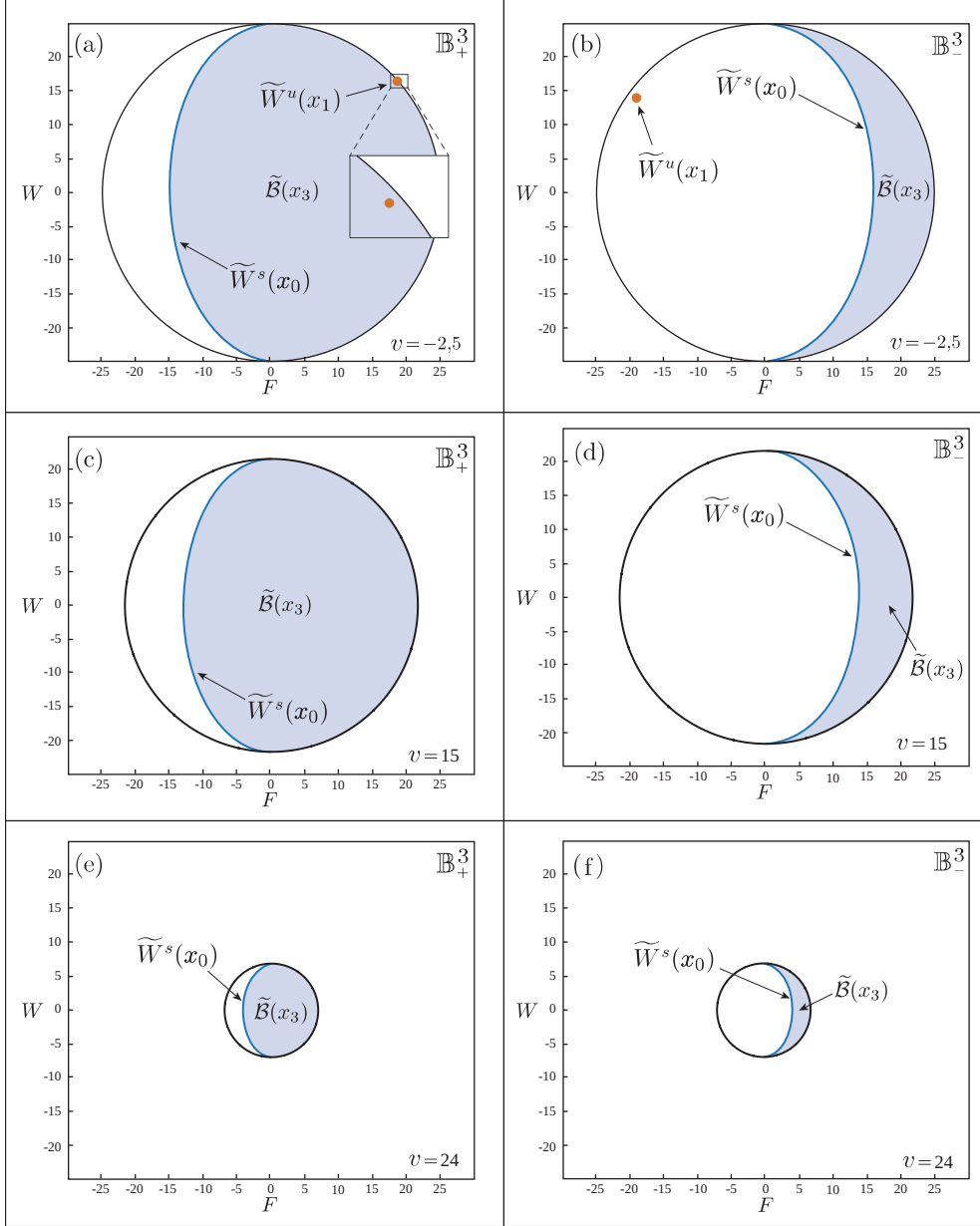
FIG. 18. *The organization of basins of attraction and invariant objects of* (22) *around* x_0. *Each relevant object in each hemisphere of* $\mathbb{S}^3$ *is seen in cross sections* $\Sigma_v = \{(F, W, V_F, V_W) \in \mathbb{R}^4 : V_W = v\}$ *for* $v = -2.5$ *in panels (a)-(b),* $v = 15$ *in panels (c)-(d), and* $v = 24$ *in panels (e)-(f). The shaded region* $\widetilde{\mathcal{B}}(x_3)$ *corresponds to points in the basin of attraction* $\mathcal{B}(x_3)$ *of* x_3*, while the white region is the basin of attraction of infinity.*

or to infinity; the exception is the heteroclinic orbit γ_{1-0} found above.

7. Discussion. We have investigated strategies to deal with dengue propagation, based on the introduction of the bacterium *Wolbachia* into a population of *Aedes aegypti* mosquitoes. Our study was two-fold. First, we considered the competition model (1) proposed in [14] for the interaction

between wild and *Wolbachia*-infected mosquitoes. By studying the relevant invariant manifolds that form the basin boundaries of interest, we characterize a threshold value w^s for the human introduction of *Wolbachia*-infected mosquitoes. Beyond this threshold, the natural dynamics of the population interaction ensures the long term replacement of wild mosquitoes by infected ones. Hence, this strategy focuses on getting such desired population replacement with a minimum amount of released infected mosquitoes, i.e., to characterize the possible ways the threshold w^s can be minimized.

A continuation procedure of invariant manifolds allowed us to follow w^s with respect to parameters and obtain graphical representations of $\min(w^s)$ in terms of Ψ_F and δ_F, the birth and death rates of wild mosquitoes. Our findings indicate that the minimum values of w^s follow a hyperbola-shaped curve in the (Ψ_F, δ_F)-plane, but the actual values of $\min(w^s)$ do not vary significantly as Ψ_F and δ_F are moved. In turn, the possible minima of w^s are highly sensitive to variations on $R_W = \Psi_W - \delta_W$, i.e., the difference between the birth and death rates of *Wolbachia*-infected mosquitoes. We conclude from the mathematical evidence that w^s is an increasing function of R_W and, hence, as R_W decreases so does the threshold w^s; see Figure 3(c1)-(c2). Thus, it is essential to obtain attested estimations of the intrinsic growth rate R_W during the artificial rearing of *Wolbachia*-carrying mosquitoes in order to assess the corresponding values of w^s. Indeed, with tools from Geometric Singular Perturbation Theory we find that if $\epsilon = \frac{R_W}{K_W} > 0$ is sufficiently small and within biologically realistic ranges, it is possible to achieve a near-extinction scenario for wild mosquitoes in a very fast way provided the initial amount of infected mosquitoes lies within a suitable range (here, K_W is the carrying capacity of infected mosquitoes). For practical purposes, this interval of initial conditions is bounded below by the threshold value w^s and above by expressions (16) or (17), provided (Ψ_F, δ_F) lie above or below, respectively, the line L defined in (12) and $\epsilon > 0$ is sufficiently small. In real-life settings, the actual position of (Ψ_F, δ_F), either above or below the line L, may depend on the temperature [82]. Therefore, the "safe" range for choosing the amount of *Wolbachia*-carrying mosquitoes to perform an initial release is $W(0) \in]w^s, \min\{p_1^W, p_2^W\}[$. In mathematical terms, a decrease of R_W or an increase of K_W would induce that $\epsilon \to 0$. However, from the biological standpoint, the decrease of $R_W = \Psi_W - \delta_W$ implies a further reduction of individual fitness of *Wolbachia*-carrying mosquitoes which is already affected by the presence of *Wolbachia*. On the other hand, the increase of K_W can be reached by performing the releases close to the areas with abundant resources for mosquito survival and reproduction, since K_W effectively stands for the maximal number of *Wolbachia*-carrying mosquitoes supported by the environment. In fact, the numerical evidence suggests that in (13) we actually have $\inf(w^s) = \min(m) = 314$ in the singular limit $\epsilon \to 0$ along the line L, which is only slightly higher than $K_W = 300$. Hence, the line L is also relevant in that it represents a condition on parameters that facilitates the chance of the threshold w^s to be smaller; see also Figure 3. Moreover, we conclude that the value of $\inf(w^s)$ could be further decreased if the carrying capacity K_F decreases or if the Allee threshold parameter K_0 is increased (with both parameters being related to the evolution of the wild mosquitoes). In practical terms, the reduction of K_F is hard to attain, while a temporary increase of K_0 can be reached by the application of chemical substances (such as larvicides and insecticides) prior to inundative release of *Wolbachia*-carriers. In conclusion, the strategy of analyzing w^s as a point in a stable manifold suggests a population replacement in a more efficient way in terms of both the number of infected mosquitoes released and the time needed to lower the wild mosquitoes population.

In the second part of this work we studied an extension of (1) in which both populations are allowed to move on a one-dimensional spatial domain. The result was a set of reaction-diffusion equations on which we characterized traveling wave solutions with an approach from invariant manifold analysis. More concretely, we identified the traveling fronts as heteroclinic orbits in a four-dimensional vector field and assessed the minimal wave speed $c_{min} = c_1^*$ expressed as a function of the diffusion coefficient (see (31)). To do so, after a study of local properties of the system, we computed global stable and unstable manifolds of dimensions one, two, and three, and searched for the intersections between them. We even proposed a new method to calculate and visualize three-dimensional manifolds of four-dimensional vector fields which, as far as we know, is the first of its kind. The collected

evidence indicates the existence of uncountably many heteroclinic connections associated with wave fronts exhibiting the desired population replacement. While numerical experiments (not shown in this work) suggest that these infinitely many traveling waves may be unstable —hence, hard to find by standard methods, and yet very abundant!—, all the associated heteroclinic connections are structurally stable phenomena. Namely, the intersections of related global invariant manifolds in $\mathbb{R}^4$ are transverse and associated with hyperbolic equilibria. The biological importance of this result is that dynamical systems theory ensures that the corresponding traveling fronts persist under variation in an open set of the model parameters.

All in all, these results emerge as valuable insight into the population replacement strategy applied to our model. Notice that this work is also useful in that it shows the scope of what can be achieved in nonlinear dynamics with a combination of bifurcation theory, advanced numerical techniques for dynamical systems, and invariant manifold analysis. For instance, similar techniques can be applied to study a more sophisticated model of interaction between wild and *Wolbachia*-infected male and female mosquitoes [15]; our resulting model is a four-dimensional vector field in which the basin of attraction of the full *Wolbachia* invasion equilibrium is given by a three-dimensional stable manifold which acts, effectively, as the threshold for a potential release campaign of modified mosquitoes.

On the other hand, one can also consider alternative ways to model the spatial movement of mosquitoes. Indeed, some evidence indicates that this dispersal —at an individual scale— may not be random [64]. Under this assumption, more general versions of diffusion should be considered [55].

8. Appendix. Here we briefly review some of the relevant concepts on Geometric Singular Perturbation Theory (GSPT) for slow-fast systems, also known as Fenichel Theory, as needed for section 3.3. For further details see, for instance [26, 39, 45] and the references therein; for GSPT applied to biology see [34]. Let $0 < \epsilon = \frac{R_W}{K_W} \ll 1$ in (1). With this notation, we can express (1) in the following form:

$$(37) \qquad \begin{cases} F' &= M(F,W) := Fh(F,W), \\ W' &= \epsilon \left[K_W W - (F+W)W \right]. \end{cases}$$

Here, the derivatives on the left hand side of the equations are with respect to time on the fast time scale τ, and the function h is given by

$$(38) \qquad h(F,W) = \left[\Psi_F - \frac{R_F}{K_F}(F+W) \right] \left(\frac{F}{K_0} - 1 \right) - \delta_F.$$

The parameter $0 < \epsilon \ll 1$ corresponds to the ratio of time scales, so that F behaves as the fast variable and W as the slow one; the variable W evolves ϵ times slower than F. One can easily rescale time by ϵ in (37) and write (1) as

$$(39) \qquad \begin{cases} \epsilon \dot{F} &= M(F,W), \\ \dot{W} &= K_W W - (F+W)W, \end{cases}$$

where the derivatives are now with respect to time on the slow time scale t; note that $t = \epsilon \tau$ and systems (37) and (39) are equivalent as long as $\epsilon \neq 0$. Solutions of slow-fast systems can be thought of as a concatenation of slow motion with fast segments. The fast and slow dynamics of (1) are described, respectively, by systems (37) and (39), respectively. For $\epsilon > 0$ small, these systems are approximated, respectively, by the limiting systems

$$(40) \qquad \begin{cases} F' &= M(F,W), \\ W' &= 0, \end{cases}$$

and

$$(41) \qquad \begin{cases} 0 &= M(F,W), \\ \dot{W} &= K_W W - (F+W)W, \end{cases}$$

obtained from the singular limit $\epsilon \to 0$ of (37) and (39), respectively, in the corresponding time scale. System (37) is known as the *fast subsystem* or *layer equations*, whereas (39) is known as the *slow flow* or *reduced system*. Systems (40) and (41) are no longer equivalent, but one can use this slow-fast splitting to approximate the dynamics of the full system (37) or (39) for $\epsilon > 0$. That is one of the main goals of GSPT.

The switching between slow and fast motion of trajectories is organized by the so-called *critical manifold*:

$$S = \{(F, W) \in \mathbb{R}^2_+ : M(F, W) = 0\},$$

which is the nullcline of the fast variable F. The fast dynamics takes place off the set S, while the slow dynamics corresponds to the flow restricted to S. In this formulation, from (39), the set S corresponds to the union of the axis $S^1 := \{F = 0\}$ and the hyperbola $h(F, W) = 0$ whose axes are spanned by the vectors $(1 + \sqrt{2}, 1)$ and $(1 - \sqrt{2}, 1)$ at its center. A direct calculation shows that the branches of this hyperbola correspond to S^2 and the curve $S^3 = \{W = N(F)\}$ defined by (9) and plotted in orange color in Figures 2, 4 and 5 . The set S gives a constraint for the limiting slow motion (41) and corresponds to a manifold of equilibria for the limiting fast motion. The set S can have attracting or repelling branches with respect to (40). These different branches are separated by *fold points* on S, which are defined by solutions of the system of algebraic equations:

$$M(F, W) = Fh(F, W) = 0, \qquad \frac{\partial M}{\partial F} = h + F\frac{\partial h}{\partial F} = 0,$$

provided that $\dfrac{\partial^2 M}{\partial F^2} \neq 0$. At a fold point, the critical manifold undergoes a saddle-node bifurcation as a manifold of equilibria of system (40), the fast flow is tangent to the critical manifold, and in this setting with one fast and one slow variable, attracting and repelling branches of the critical manifold meet.

Fold points along S^1, i.e., the W-axis $\{F = 0\}$, must satisfy $h(0, W) = 0$. The only point satisfying this condition is $p_1 = (0, p_1^W)$, where $p_1^W = \frac{K_F(\Psi_F + \delta_F)}{\Psi_F - \delta_F}$. However, p_1 is not a fold point in a geometrical sense since S^1 is a straight line. Rather, p_1 simply signals a change of stability of points in S^1 with respect to the fast dynamics.

Along the hyperbola $h(F, W) = 0$ we have fold points if $F\frac{\partial h}{\partial F} = 0$. In this case, we obtain the fold points $p_2 = (p_2^F, p_2^W) \in S^2$ and $p_m = (F_m, m) \in S^3$, where

$$
\begin{array}{rcl}
p_2^F & = & K_0 - \sqrt{\frac{K_F K_0 \delta_F}{\Psi_F - \delta_F}}, \\[2mm]
p_2^W & = & \frac{-(\Psi_F - \delta_F)K_0 + \Psi_F K_F + 2\sqrt{\delta_F K_0 K_F(\Psi_F - \delta_F)}}{\Psi_F - \delta_F}, \\[2mm]
F_m & = & K_0 + \sqrt{\frac{K_F K_0 \delta_F}{\Psi_F - \delta_F}},
\end{array}
$$

and

$$m = \frac{-(\Psi_F - \delta_F)K_0 + \Psi_F K_F - 2\sqrt{\delta_F K_0 K_F(\Psi_F - \delta_F)}}{\Psi_F - \delta_F}.$$

Note that conditions (2) and (5) imply $p_2^F < F_m$ and $m < p_2^W \leq p_1^W$. The location of p_2 depends on the sign of p_2^F. In that sense, it is easy to check that $p_2^F > 0$ (i.e., p_2 is in the first quadrant) if and only if $\delta_F < \frac{K_0}{K_0 + K_F}\Psi_F$. If $\delta_F = \frac{K_0}{K_0 + K_F}\Psi_F$ the points p_1 and p_2 collide; we do not address this issue here since it is out if the scope of this paper.

Fast dynamics. In system (40), the critical manifold S is a manifold of equilibria. Its stability depends on the sign of $\frac{\partial M}{\partial F} = h + F\frac{\partial h}{\partial F}$. From (38), at points on $S^2 \cup S^3 = \{h(F, W) = 0\}$ with $F > 0$, the fast dynamics is reduced to the study of the sign of

$$\frac{\partial h}{\partial F} = -\frac{\Psi_F - \delta_F}{K_F} + \left(\Psi_F - \frac{\Psi_F - \delta_F}{K_F}(F + W)\right)\frac{1}{K_0}.$$

The set $\frac{\partial h}{\partial F} = 0$ corresponds to a straight line through the fold points $p_2 \in S^2$ and $p_m \in S^3$ in the (F, W)-plane. This line divides the first quadrant into two half-planes. On the upper one, we have $\frac{\partial h}{\partial F} < 0$, while $\frac{\partial h}{\partial F} > 0$ on the lower one. It follows that the stability of the set S is as in Figure 4(a) or Figure 5(a) according to the following statement:

RESULT 4. *In* (40) *the stability of the branches of S in the first quadrant is the following:*
1. *Stability of S^1: The segment $0 < W < p_1^W$ on S^1 is attracting, and the ray $W > p_1^W$ is repelling.*
2. *Stability of S^2: If $\delta_F > \frac{K_0}{K_0 + K_F}\Psi_F$, S^2 is attracting. On the other hand, if $\delta_F < \frac{K_0}{K_0 + K_F}\Psi_F$, the segment of S^2 between p_1 and p_2 is repelling, and the remaining branch is attracting.*
3. *Stability of S^3: The segment S^r between x_3 and p_m is repelling, and the segment S^a between p_m and x_4 is attracting.*

Slow dynamics. Let us consider system (41) to study the flow on the critical manifold S. Along S^1 we have the restricted one-dimensional system $\dot{W} = (K_W - W)W$ with two equilibria at $W = 0$ and $W = K_W$. It follows that $W = 0$ is repelling and $W = K_W$ is attracting. Note that these equilibria correspond to x_0 and x_1, respectively, in the full system.

To study the flow on the hyperbola $S^2 \cup S^3 = \{h(F, W) = 0\}$, let us differentiate the first equation of (41) to obtain

$$0 = \frac{\partial M}{\partial t} = \frac{\partial (Fh)}{\partial F}\dot{F} + \frac{\partial (Fh)}{\partial W}\dot{W}.$$

Or equivalently,

$$\left(h + F\frac{\partial h}{\partial F}\right)\dot{F} = -F\frac{\partial h}{\partial W}\dot{W}.$$

Along $S^2 \cup S^3$ we have $h = 0$, and considering $F > 0$, we get

$$\frac{\partial h}{\partial F}\dot{F} = -\frac{\partial h}{\partial W}\dot{W}.$$

Notice that from (38) we have

$$\frac{\partial h}{\partial W} = -\frac{\Psi_F - \delta_F}{K_F K_0}(F - K_0),$$

and

$$(42) \qquad W|_{S^2 \cup S^3} = \frac{(\Psi_F K_F - (\Psi_F - \delta_F)F)(F - K_0) - \delta_F K_F K_0}{(F - K_0)(\Psi_F - \delta_F)}.$$

Note that the straight line $\{F = K_0\}$ does not cross h. Hence, the slow flow along $S^2 \cup S^3$ can be expressed in (F-dependent) local charts as

$$(43) \qquad \frac{\partial h}{\partial F}\dot{F} = \frac{\Psi_F - \delta_F}{K_F K_0}(F - K_0)(K_W - (F + W))W,$$

where W is as in (42). The slow flow becomes singular at fold points —i.e., $\frac{\partial h}{\partial F} = 0$—, but it can be desingularized by rescaling time with the factor $-\frac{\partial h}{\partial F}$. This allows the extension of (43) to fold points in the form

$$(44) \qquad \dot{F} = -\frac{\Psi_F - \delta_F}{K_F K_0}(F - K_0)(K_W - (F + W))W.$$

System (44) is known as the *desingularized reduced system*. Note that this time rescaling reverses the direction of the flow on the repelling sheets of $S^2 \cup S^3$, that is between x_3 and p_m in S^3 and between p_1 and p_2 in S^2 if $\delta_F < \frac{K_0}{K_0+K_F}\Psi_F$ (i.e. $p_2^F > 0$); if $\delta_F > \frac{K_0}{K_0+K_F}\Psi_F$ (i.e. $p_2^F < 0$), there is no repelling branch of S^2 in the first quadrant. Substitution of (42) into (44) gives us the explicit desingularized slow flow in the following form:

$$(45) \qquad \dot{F} = \frac{\left(\delta_F K_F K_0 + (F-K_0)(FR_F - K_F \Psi_F)\right)\left(\delta_F K_F K_0 - (F-K_0)(K_F \Psi_F - K_W R_F)\right)}{R_F K_F K_0 (F-K_0)},$$

where $R_F = \Psi_F - \delta_F$. The equilibria of (45) are $F = K_b$, $F = F_c$, $F = K_*$ in S^3 (corresponding to x_3, x_2 and x_4, respectively, in the full system). By analyzing the one-dimensional system (45), considering the time reversal along the repelling branches of h and returning to (43), we obtain the stability of the equilibria along $S_2 \cup S_3$ in the first quadrant. It follows that the slow flow along the critical manifold in (41) is as in Figure 4(a) or Figure 5(a). More precisely, we have the following:

RESULT 5. *Let us consider the set $\mathbb{R}^2$ restricted to the first quadrant and the coordinates axes. In system (41) the dynamics on S is completely determined as follows:*
1. *In S^1 the point $W = 0$ is repelling, and $W = K_W$ is attracting. Moreover, $\dot{W} < 0$ for every regular point in S^1 with $W > K_W$.*
2. *There are no equilibria in S^2. However, the desingularization in system (43) in order to obtain (44) implies that $\dot{F} > 0$ for $F \in (0, p_2^F)$ and $\dot{F} < 0$ for $F \in (p_2^F, \infty)$ in S^2.*
3. *In S^3 the point $F = K_b$ is repelling, $F = F_c$ is attracting, and $F = K_*$ is attracting.*

Once having a full description of the slow and fast dynamics in the limiting systems (40) and (41), we can use it to understand the dynamics in the full system for $\epsilon > 0$ small. The key is to use the critical manifold as a switch between slow and fast motion of trajectories. This is one of the main results in Fenichel theory, which guarantees that attracting and repelling branches of the critical manifold perturb to attracting and repelling slow manifolds, respectively, provided that a condition known as normal hyperbolicity is satisfied. In generic systems, normal hyperbolicity is traduced as hyperbolicity of the critical manifold as a manifold of equilibria of the fast subsystem. For system (37)—and equivalently (39)—, the normal hyperbolicity of the critical manifold is lost at its fold points. Therefore, slow manifolds are $O(\epsilon)$ perturbations of the critical manifold away from fold points; slow manifolds are as smooth as the critical manifold and have the same stability properties of its normally hyperbolic branches. Slow manifolds are not unique, but two slow manifolds of the same type are $O(\exp(-K/\epsilon))$ close to each other, for some $K > 0$ [39]. Slow manifolds govern the slow motion of trajectories of the singularly perturbed system for $\epsilon > 0$, since they correspond to solutions that remain slow for an $O(1)$ time on the slow timescale. In particular, for $\epsilon > 0$ the saddle equilibrium point x_2 persists and keeps its stability. Its one-dimensional stable manifold $W^s(x_2)$ has a passage through a fast fiber, approaches the fold point p_1 and then lies $O(\epsilon)$ close to S^r, following a repelling slow manifold S^r_ϵ.

REFERENCES

[1] *Mosquito World Program.* https://www.worldmosquitoprogram.org/. Accessed: 2019-12-16.
[2] P. AGUIRRE, *Bifurcations of two-dimensional global invariant manifolds near a noncentral saddle-node homoclinic orbit*, SIAM J. Appl. Dyn. Syst., 14 (2015), pp. 1600–1643.
[3] P. AGUIRRE, E. DOEDEL, B. KRAUSKOPF, AND H. M. OSINGA, *Investigating the consequences of global bifurcations for two-dimensional invariant manifolds of vector fields*, Discr. Cont. Dynam. Syst., 29 (2010), pp. 1309–1344.
[4] P. AGUIRRE, B. KRAUSKOPF, AND H. M OSINGA, *Global invariant manifolds near homoclinic orbits to a real saddle:(non) orientability and flip bifurcation*, SIAM J. Appl. Dynam. Syst., 12 (2013), pp. 1803–1846.

[5] P. Aguirre, B. Krauskopf, and H. M. Osinga, *Global invariant manifolds near a Shilnikov homoclinic bifurcation*, J. Comput. Dynam., 1 (2014), pp. 1–38.

[6] M. M. Akiner, B. Demirci, G. Babuadze, V. Robert, and F. Schaffner, *Spread of the invasive mosquitoes Aedes aegypti and Aedes albopictus in the Black Sea region increases risk of chikungunya, dengue, and zika outbreaks in europe*, PLoS Negl. Trop. Dis., 10 (2016), pp. 1–5.

[7] L. Alphey, M. Benedict, R. Bellini, G. G. Clark, D. A. Dame, M. W. Service, and S. L. Dobson, *Sterile-insect methods for control of mosquito-borne diseases: an analysis*, Vector Borne Zoonotic Dis., 10 (2010), pp. 295–311.

[8] H. Araújo, D. Carvalho, R. Ioshino, A. Costa-da Silva, and M. Capurro, *Aedes aegypti control strategies in brazil: incorporation of new technologies to overcome the persistence of dengue epidemics*, Insects, 6 (2015), pp. 576–594.

[9] S. Bhatt, P. W. Gething, O. J. Brady, J. P. Messina, A. W. Farlow, C. L. Moyes, J. M. Drake, J. S. Brownstein, A. G. Hoen, O. Sankoh, et al., *The global distribution and burden of dengue*, Nature, 496 (2013), p. 504.

[10] P.-A. Bliman, M. S. Aronna, F. C. Coelho, and M. Da Silva, *Ensuring successful introduction of wolbachia in natural populations of aedes aegypti by means of feedback control*, J. Math. Biol., 76 (2018), pp. 1269–1300.

[11] P.-A. Bliman, D. Cardona-Salgado, Y. Dumont, and O. Vasilieva, *Implementation of control strategies for sterile insect techniques*, Math. Biosci., 314 (2019), pp. 43 – 60.

[12] P.-A. Bliman and N. Vauchelet, *Establishing traveling wave in bistable reaction-diffusion system by feedback*, IEEE Control Syst. Lett., 1 (2017), pp. 62–67.

[13] N. F. Britton, *Essential Mathematical Biology*, Springer Science & Business Media, 2012.

[14] D. E. Campo-Duarte, D. Cardona-Salgado, and O. Vasilieva, *Establishing wMelPop Wolbachia infection among wild Aedes aegypti females by optimal control approach*, Appl. Math. Inf. Sci., 11 (2017), pp. 1011–1027.

[15] D. E Campo-Duarte, O. Vasilieva, D. Cardona-Salgado, and M. Svinin, *Optimal control approach for establishing wMelPop Wolbachia infection among wild Aedes aegypti populations*, J. Math. Biol., 76 (2018), pp. 1907–1950.

[16] A. R. Champneys, Yu. A. Kuznetsov, and B. Sandstede, *A numerical toolbox for homoclinic bifurcation analysis*, Int. J. Bifurcat. Chaos, 6 (1996), pp. 867–887.

[17] M. H. T. Chan and P. S Kim, *Modelling a Wolbachia invasion using a slow–fast dispersal reaction–diffusion approach*, Bull. Math. Biol., 75 (2013), pp. 1501–1523.

[18] D. Contreras-Julio and P. Aguirre, *Allee thresholds and basins of attraction in a predation model with double Allee effect*, Math. Methods Appl. Sci., 41 (2018), pp. 2699–2714.

[19] C. De Boor and B. Swartz, *Collocation at Gaussian points*, SIAM J. Num. Anal., 10 (1973), pp. 582–606.

[20] A. Dhooge, W. Govaerts, and Yu. A. Kuznetsov, *MATCONT: a MATLAB package for numerical bifurcation analysis of ODEs*, ACM T. Math. Software, 29 (2003), pp. 141–164.

[21] S. L. Dobson, C. W. Fox, and F. M. Jiggins, *The effect of Wolbachia-induced cytoplasmic incompatibility on host population size in natural and manipulated systems*, P. Roy. Soc. B Biol. Sci., 269 (2002), pp. 437–445.

[22] E. J. Doedel, T. F. Fairgrieve, B. Sandstede, A. R. Champneys, Y. A. Kuznetsov, and X. Wang, *Auto-07p: Continuation and bifurcation software for ordinary differential equations*, (2007).

[23] I. Dorigatti, C. McCormack, G. Nedjati-Gilani, and N. Ferguson, *Using Wolbachia for dengue control: Insights from modelling*, Trends in Parasitology, 34 (2018), pp. 102–113.

[24] H. L. C. Dutra, M. N. Rocha, F. B. S. Dias, S. B. Mansur, E. P. Caragata, and L. A. Moreira, *Wolbachia blocks currently circulating zika virus isolates in Brazilian Aedes aegypti mosquitoes*, Cell Host Microbe, 19 (2016), pp. 771–774.

[25] V. A. Dyck, J. Hendrichs, and A. S. Robinson, *Sterile Insect Technique: Principles and Practice in Area-wide Integrated Pest Management*, Springer, 2006.

[26] N. Fenichel, *Geometric singular perturbation theory for ordinary differential equations*, J. Differ. Equations, 31 (1979), pp. 53–98.

[27] N. Ferguson, D. Kien, H. Clapham, R. Aguas, V. Trung, T. Chau, J. Popovici, P. Ryan, S. ONeill, E. McGraw, V. Long, L. Dui, H. Nguyen, N. Vinh Chau, B. Wills, and C. Simmons, *Modeling the impact on virus transmission of Wolbachia-mediated blocking of dengue virus infection of Aedes aegypti*, Sci. Transl. Med., 7 (2015), pp. 279ra37–279ra37.

[28] Centers for Disease Control, Prevention, et al., *Prevention of specific infectious diseases*, in CDC Health Information for International Travel 2008, Elsevier, Philadelphia, PA, 2008, pp. 114–362.

[29] D. J. Gubler, *Epidemic dengue/dengue hemorrhagic fever as a public health, social and economic problem in the 21st century.*, Trends Microbiol., 10 (2002), pp. 100–3.

[30] J. Guckenheimer and P. Holmes, *Nonlinear Oscillations, Dynamical Systems, and Bifurcations of Vector Fields*, Applied Mathematical Sciences, Springer New York, 2002.

[31] J. Guckenheimer, B. Krauskopf, H. M. Osinga, and B. Sandstede, *Invariant manifolds and global bifurcations*, Chaos, 25 (2015), p. 097604.

[32] J. Guckenheimer and A. Vladimirsky, *A fast method for approximating invariant manifolds*, SIAM J. Appl.

Dynam. Syst., 3 (2004), pp. 232–260.

[33] A. HARO, M. CANADELL, J.-L. FIGUERAS, A. LUQUE, AND J.-M. MONDELO, *The Parameterization Method for Invariant Manifolds*, Springer, 2016.

[34] G. HEK, *Geometric singular perturbation theory in biological practice*, J. Math. Biol., 60 (2010), pp. 347–386.

[35] C.-H. HSU, C.-R. YANG, T.-H. YANG, AND T.-S. YANG, *Existence of traveling wave solutions for diffusive predator–prey type systems*, J. Differ. Equat., 252 (2012), pp. 3040–3075.

[36] L. HU, M. TANG, Z. WU, Z. XI, AND J. YU, *The threshold infection level for Wolbachia invasion in random environments*, J. Differ. Equat., 266 (2019), pp. 4377–4393.

[37] J. HUANG, S. RUAN, P. YU, AND Y. ZHANG, *Bifurcation analysis of a mosquito population model with a saturated release rate of sterile mosquitoes*, SIAM J. Appl. Dynam. Syst., 18 (2019), pp. 939–972.

[38] M. HUANG, J. YU, L. HU, AND B. ZHENG, *Qualitative analysis for a Wolbachia infection model with diffusion*, Sci. China Math., 59 (2016), pp. 1249–1266.

[39] C. JONES, *Geometric singular perturbation theory*, in Dynamical systems, Springer, 1995, pp. 44–118.

[40] J. KAMTCHUM-TATUENE, B. L. MAKEPEACE, L. BENJAMIN, M. BAYLIS, AND T. SOLOMON, *The potential role of Wolbachia in controlling the transmission of emerging human arboviral infections*, Curr. Opin. Infect. Dis., 30 (2017), p. 108.

[41] B. KRAUSKOPF AND H. M. OSINGA, *Computing invariant manifolds via the continuation of orbit segments*, in Numerical Continuation Methods for Dynamical Systems, Springer, 2007, pp. 117–154.

[42] B. KRAUSKOPF, H. M. OSINGA, E. J. DOEDEL, M. E. HENDERSON, J. GUCKENHEIMER, A. VLADIMIRSKY, M. DELL-NITZ, AND O. JUNGE, *A survey of method's for computing (un)stable manifolds of vector fields*, Int. J. Bifurc. Chaos Appl. Sci. Eng., 15 (2005), pp. 763–791.

[43] B. KRAUSKOPF AND T. RIESS, *A Lin's method approach to finding and continuing heteroclinic connections involving periodic orbits*, Nonlinearity, 21 (2008), p. 1655.

[44] M. KRUPA AND P. SZMOLYAN, *Extending geometric singular perturbation theory to nonhyperbolic points—fold and canard points in two dimensions*, SIAM J. Math. Anal., 33 (2001), pp. 286–314.

[45] C. KUEHN, *Multiple Time Scale Dynamics*, Springer, 2015.

[46] YU. A KUZNETSOV, *Elements of Applied Bifurcation Theory*, Springer Science & Business Media, 2013.

[47] D. LI AND H. WAN, *The threshold infection level for Wolbachia invasion in a two-sex mosquito population model*, Bull. of Math. Biol., (2019).

[48] J. N. LILES ET AL., *Effects of mating or association of the sexes on longevity in Aedes aegypti (l.)*, Mosq. News, 25 (1965), pp. 434–9.

[49] X. LIN, P. WENG, AND C. WU, *Traveling wave solutions for a predator–prey system with sigmoidal response function*, J. Dyn. Diff. Equ., 23 (2011), pp. 903–921.

[50] X.-B. LIN, *Using Melnikov's method to solve Silnikov's problems*, Proc. R. Soc. Edinb. A, 116 (1990), pp. 295–325.

[51] N. A. MAIDANA AND H. M. YANG, *Describing the geographic spread of dengue disease by traveling waves*, Math. Biosci., 215 (2008), pp. 64–77.

[52] C. J. MCMENIMAN, R. V. LANE, B. N. CASS, A. W. C. FONG, M. SIDHU, Y.-F. WANG, AND S. L. O'NEILL, *Stable introduction of a life-shortening Wolbachia infection into the mosquito aedes aegypti*, Science, 323 (2009), pp. 141–144.

[53] C. J. MCMENIMAN AND S. L. O'NEILL, *A virulent Wolbachia infection decreases the viability of the dengue vector Aedes aegypti during periods of embryonic quiescence*, PLoS Negl. Trop. Dis., 4 (2010), p. e748.

[54] L. MOREIRA, I. ITURBE-ORMAETXE, J. JEFFERY, A. LU, G AND. PYKE, L. HEDGES, B. ROCHA, S. HALL-MENDELIN, A. DAY, M. RIEGLER, L. HUGO, K. JOHNSON, B. KAY, E. MCGRAW, A. VAN DEN HURK, P. RYAN, AND S. ONEILL, *A Wolbachia symbiont in Aedes aegypti limits infection with dengue, chikungunya, and plasmodium*, Cell, 139 (2009), pp. 1268–1278.

[55] J. D. MURRAY, *Mathematical Biology*, Springer, 2002.

[56] M. Z. NDII, R. I. HICKSON, D. ALLINGHAM, AND G. N. MERCER, *Modelling the transmission dynamics of dengue in the presence of Wolbachia*, Math. Biosci., 262 (2015), pp. 157–166.

[57] WORLD HEALTH ORGANIZATION ET AL., *Dengue and severe dengue*, tech. report, World Health Organization. Regional Office for the Eastern Mediterranean, 2014.

[58] H. M. OSINGA, *Two-dimensional invariant manifolds in four-dimensional dynamical systems*, Comput. Graph., 29 (2005), pp. 289–297.

[59] J. PATTERSON, M. SAMMON, AND M. GARG, *Dengue, zika and chikungunya: Emerging arboviruses in the new world*, West. J. Emerg. Med., 17 (2016), p. 671.

[60] J. POPOVICI, L. A. MOREIRA, A. POINSIGNON, I. ITURBE-ORMAETXE, D. MCNAUGHTON, AND S. L. O'NEILL, *Assessing key safety concerns of a Wolbachia-based strategy to control dengue transmission by Aedes mosquitoes*, Mem. Inst. Oswaldo Cruz, 105 (2010), pp. 957–964.

[61] J. L. RASGON AND T. W. SCOTT, *An initial survey for Wolbachia (Rickettsiales: Rickettsiaceae) infections in selected California mosquitoes (Diptera: Culicidae)*, J. Med. Entomol., 41 (2004), pp. 255–257.

[62] S. RITCHIE, M. TOWNSEND, C. PATON, A. CALLAHAN, AND A. HOFFMANN, *Application of wMelPop Wolbachia strain to crash local populations of Aedes aegypti*, PLoS Negl. Trop. Dis., 9 (2015), p. e0003930.

[63] P. A. ROSS, N. M. ENDERSBY, H. L. YEAP, AND A. A. HOFFMANN, *Larval competition extends developmental time*

and decreases adult size of wMelPop Wolbachia-infected Aedes aegypti, Am. J. Trop. Med. Hyg., 91 (2014), pp. 198–205.

[64] R. C. RUSSELL, C. E. WEBB, C. R. WILLIAMS, AND S. A. RITCHIE, *Mark–release–recapture study to measure dispersal of the mosquito Aedes aegypti in Cairns, Queensland, Australia*, Med. Vet. Entomol., 19 (2005), pp. 451–457.

[65] J. L. SAN MARTN, O. BRATHWAITE, B. ZAMBRANO, J. O. SOLRZANO, A. BOUCKENOOGHE, G. H. DAYAN, AND M. G. GUZMN, *The epidemiology of dengue in the Americas over the last three decades: A worrisome reality*, Am. J. Trop. Med. Hyg., 82 (2010), pp. 128–135.

[66] B. SANDSTEDE, *Constructing dynamical systems having homoclinic bifurcation points of codimension two*, J. Dyn. Differ. Equ., 9 (1997), pp. 269–288.

[67] T. L. SCHMIDT, I. FILIPOVIĆ, A. A. HOFFMANN, AND G. RAŠIĆ, *Fine-scale landscape genomics helps explain the slow spatial spread of Wolbachia through the Aedes aegypti population in Cairns, Australia*, Heredity, 120 (2018), p. 386.

[68] L. P. SHILNIKOV, A. SHILNIKOV, D. TURAEV, AND L. CHUA, *Methods of Qualitative Theory in Nonlinear Dynamics. Part II.*, 2001.

[69] J. SOTOMAYOR, *Licões de Equacões Diferenciais Ordinárias*, Instituto de Matemática Pura e Aplicada, CNPq, 1979.

[70] S. H STROGATZ, *Nonlinear Dynamics and Chaos: With Applications to Physics, Biology, Chemistry, and Engineering*, CRC Press, 2018.

[71] L. T. TAKAHASHI, N. A. MAIDANA, W. C. FERREIRA, P. PULINO, AND H. M. YANG, *Mathematical models for the Aedes aegypti dispersal dynamics: travelling waves by wing and wind*, Bull. Math. Biol., 67 (2005), pp. 509–528.

[72] C. TIAN AND S. RUAN, *A free boundary problem for Aedes aegypti mosquito invasion*, Appl. Math. Model., 46 (2017), pp. 203–217.

[73] V. M. TIKHOMIROV, *A study of the diffusion equation with increase in the amount of substance, and its application to a biological problem*, in Selected Works of A. N. Kolmogorov, Springer, 1991, pp. 242–270.

[74] F. TOPPUTO, *Fast numerical approximation of invariant manifolds in the circular restricted three-body problem*, Commun. Nonlinear Sci. Numer., 32 (2016), pp. 89–98.

[75] M. TURELLI, *Cytoplasmic incompatibility in populations with overlapping generations*, Evolution Int. J. Org. Evolution., 64 (2010), pp. 232–241.

[76] M. TURELLI AND N. H. BARTON, *Deploying dengue-suppressing Wolbachia: Robust models predict slow but effective spatial spread in Aedes aegypti*, Theor. Popul. Biol., 115 (2017), pp. 45–60.

[77] A. I. VOLPERT, V. A. VOLPERT, AND V. A. VOLPERT, *Traveling Wave Solutions of Parabolic Systems*, American Mathematical Soc., 1994.

[78] T. WALKER, P. JOHNSON, L. MOREIRA, I. ITURBE-ORMAETXE, F. FRENTIU, C. MCMENIMAN, Y. LEONG, Y. DONG, J. AXFORD, P. KRIESNER, A. LLOYD, S. RITCHIE, S. ONEILL, AND A. HOFFMANN, *The wMel Wolbachia strain blocks dengue and invades caged Aedes aegypti populations*, Nature, 476 (2011), pp. 450–453.

[79] M. WOOLFIT, I. ITURBE-ORMAETXE, T. BROWNLIE, J. C.AND WALKER, M. RIEGLER, A. SELEZNEV, J. POPOVICI, E. RANCÈS, B. A. WEE, J. PAVLIDES, ET AL., *Genomic evolution of the pathogenic Wolbachia strain, wMelPop*, Genome Biol. Evol., 5 (2013), pp. 2189–2204.

[80] J. XIN, *Front propagation in heterogeneous media*, SIAM Review, 42 (2000), pp. 161–230.

[81] W. M. S YAMASHITA, L. T. TAKAHASHI, AND G. CHAPIRO, *Traveling wave solutions for the dispersive models describing population dynamics of Aedes aegypti*, Math. Comput. Simulat., 146 (2018), pp. 90–99.

[82] H. YANG, M. MACORIS, K. GALVANI, M. ANDRIGHETTI, AND D. WANDERLEY, *Assessing the effects of temperature on the population of Aedes aegypti, the vector of dengue*, Epidemiology & Infection, 137 (2009), pp. 1188–1202.

[83] B. ZHENG, M. TANG, J. YU, AND J. QIU, *Wolbachia spreading dynamics in mosquitoes with imperfect maternal transmission*, J. Math. Biol., 76 (2018), pp. 235–263.